Sonoelectrochemical Synthesis of metallic multilayer Nanocomposite and their Characterization

A thesis submitted
in
partial fulfillment of the requirement for the award of degree
of

Master of Technology
In
Metallurgical and Materials Engineering

Submitted
By
Rakesh Kumar Sahoo
Roll No. 20604005

Department of Metallurgical and Materials Engineering
National Institute of Technology, Rourkela
769008, May 2008

Sonoelectrochemical Synthesis of metallic multilayer Nanocomposite and their Characterization

A thesis submitted
in
partial fulfillment of the requirement for the award of degree
of

Master of Technology
In
Metallurgical and Materials Engineering

Submitted
By
Rakesh Kumar Sahoo
Roll No. 20604005

Under the Supervision of

Prof. Archana Mallick **Prof. B.C. Ray**

Department of Metallurgical and Materials Engineering
National institute of technology, Rourkela
769008, May 2008

National Institute of Technology
Rourkela

Certificate

This is to certify that the thesis entitled "**Sonoelectrochemical Synthesis of Metallic multilayer Nanocomposite and their Characterization**" submitted by Sri Rakesh Kumar Sahoo in partial fulfillment of the requirements for the award of Master of Technology in Metallurgical and Materials Engineering with specialization in "Metallurgical and Materials Engineering" at National Institute of Technology, Rourkela (Deemed University) is an authentic work carried out by him under our supervision and guidance.

To the best of our knowledge, the matter embodied in the thesis has not been submitted to any other University/Institute for the award any Degree or Diploma.

Co-supervisor
Prof. B.C. Ray
Department of Metallurgical
& Material Enginnering
National Institute of Technology,
Rourkela- 769008

Supervisor
Prof. Archana Mallick
Department of Metallurgical
& Material Engineering
National Institute of Technology,
Rourkela- 769008

Acknowledgement

I take this opportunity to express my deep regards and sincere gratitude for this valuable, expert guidance rendered to me by guide M**rs. Archana Mallick** ,Lecturer, Department of Metallurgical and Materials Engineering and **Dr. B.C.Ray** Professor, Department of Metallurgical and Materials Engineering National Institute of Technology, Rourkela. I consider me fortunate to have had opportunity to work under his guidance and enrich myself from his vast knowledge and analysis power. They will always be constant source of inspiration for me.

My sincere thanks are to Dr G.S. Agrawal, Professor and Head metallurgical and Materials Engineering Department for his talented advice and providing necessary facility for my work.

I would also take this opportunity to express my gratitude and sincere thanks to my honorable teachers Prof. A.K.Panda, Prof.B.B.Berma, Prof U.K.Mohanty and Dr.M.Kumar for their invaluable advice, constant help, encouragement, inspiration and blessings.

I would also express my sincere thanks to lab. members of Department of Metallurgical and Materials Engineering, N.I.T., Rourkela, especially, R. Pattanaik, Mr. Sameer Pradhan, U.K. Sahu for constant practical assistance and help whenever required.

Rakesh Kumar Sahoo

List of Figures

List of Tables

Abstract

Multilayers have received increasing attention in recent years because of their unique properties. These materials comprised of alternating layers of different metals and/or alloy is expected unusual and enhanced electrical, optical, magnetic and mechanical properties when the sublayer thickness is confined to the nanometer scale. In this work we tried to Cu/Ni multilayer by varying the concentration of the bath with changing potential for alternate deposition of nano multilayer. Our conclusions are the result of combining experimental work with chraterization with XRD, SEM, AFM and and nanoindentation with special concentration of the different growth texture of the multilayers grains and growth mechanism with GMR studies. We argue that this approach is the best avenue to obtain accurate information about the texture and quality of metallic multilayers. The study of physical properties of multilayers (structural, elastic, magnetic, and transport) is one of the most prosperous and rich branches of materials science today.

CONTENT

INTRODUCTION

INTRODUCTION

Since their first introduction in the early 1980s, nanocrystalline materials have been made by numerous synthesis techniques. On the basis of the underlying fundamental physical and chemical principles ,most of the more than 200 different processing routes that have been developed over the past 20 years can be classified in five distinct groups .The first three groups are vapor phase processing (e.g. physical vapor deposition ,chemical vapor deposition ,inert gas condensation),liquid phase processing's are (e.g. rapid solidification, atomization ,sonication of immiscible liquids)and solid state processing (e.g., equal channel angular pressing ,mechanical attrition ,annealing of amorphous precursors).The other two groups are chemical synthesis (e.g., sol-gel processing, inverse micelle technology)and electrochemical synthesis(e.g. electrodeposition, electroless deposition, galvaniconversion and my superior process sonoelectrochemical deposition).In many cases the later two processing routes are closely related interms of the chemical reactions involved. However the distinguishing feature of sonoelectrohemical deposition is that it involves an interface at which charge transfer occurs. Moreover ultrasound permits the refill of the double layer with metal cations and acceleration of mass transport leading to enhanced reaction rates.Secondly the ultrasound helps in reduction of particle size, homogenize the deposition without stirring of the bath.

In addition to application to decorative wear and corrosion ,erosion and oxidation resistance coatings, sonoelectrochemical deposition technology have been advanced for many different applications including large thick-walled (>1mm)electroformed products such as molds for thermoplastics composite component manufacture ,functional coating for magnetic and electronic applications, or the manufacture of microelectromechanical system components .

Electrodeposition parameters include bath composition, pH, temperature, overpotential, bath additives, etc., while important microstructural features of the substrate are grain size, crystallographic texture, dislocation density and internal stresses. Electrocrystalisation occurs either by the build-up of existing crystals or by the formation of new ones. These two processes are in computation with each other and are influenced by different factors. The two key mechanisms that have been identified as the measure

rate determining steps for nanocrystal formation are charge transfer at the electrode surface and surface diffusion of adions on the crystal surface. One of the key factors in micro structural evolution of electrodeposited in terms of the grain size and shape is inhibition ,for example resulting from reduced from surface diffusion of anions by adsorption of foreign species (such as grain refiners) on the growing surface .With increase inhibition the deposit structure changes from basis oriented and reproduction type(BR) to twin trantion types(TT),to field oriented type (FT),and finally to un-oriented dispersion type (UD).A large number of grain refiners are have been described in the literature, their effectiveness depending upon surface adsorption characteristics, compatibility with the electrolyte .

There are various applications where multilayer structure plays an important role. Especially the tribological properties of these layered structures directly depend on the layer properties, e.g., the layer thickness, surface roughness, coefficient of friction, hardness, stiffness and elastic modulus ratios of the layers to the substrate. And for quite a long time, it has been known that it was the hardness of surface and subsurface layers which are responsible for observed wear behavior. Due to these reasons, most of the earlier effort was put to synthesize structures with enhanced hardness for obtaining better wear resistance. Among various possibilities, alternate nano-laminated structure was one of them. In these structures, the strengthening is due to (a) presence of interface between two layers with wide difference in elastic modulus acts as “dislocation pinning site”. (b) The other one is substructure strengthening mechanism, and the yield strength (σ_y) depends on sublayer thickness λ as $\sigma_y \alpha \lambda^{-p}$, where p is the exponent and the mechanism changes depending upon its values; when p=1/2, the relation becomes $\sigma_y \alpha \lambda^{-1/2}$ which is nothing but Hall–Petch relationship (Hall–Petch strengthening).

Extrinsic magnetic properties play a major role in determining the performance of magnetic thin films used as magnetic recording media and magnetic sensors. These extrinsic properties are the ones which are largely determined by the microstructure of the thin magnetic films. Like other magnetoresistive effects; giant magnetoresistance (GMR) is the change in electrical resistance of some materials in response to an applied magnetic field. It was discovered that the application of a magnetic field to magnetic metallic multilayers such as Fe/Cr, Co/Cu and Ni/Cu in which ferromagnetic layers are

separated by nonmagnetic spacer layers of a few nm thick, results in a significant reduction of the electrical resistance of the multilayer. This effect was found to be much larger than other magnetoresistive effects that had ever been observed in metals and was, therefore, called “giant magnetoresistance”. In Fe/Cr, Co/Cu and Ni/Cu multilayer the magnitude of GMR can be higher than 100% at low temperatures.

Based upon the above discussion of the versatile properties and applications of multilayer metallic systems, we have made an approach to synthesize Cu/Ni multilayers with an extreme control of thickness and purity of each of the layers. Above fact has been represented in various voltametry and chronoamperometry experiments. Phase indetification and topographical information are gathered by XRD, SEM and AFM. The growth directions of the layered nanostructures are further characterized by XRD tests. Mechanical properties i.e. hardness are carried out by nanoindentation.

CHAPTER -1

Literature Survey

1. Literature Background

1.1. Mechanisms of multilayer growth

Many experimental observations revealed that there are three basic mechanisms governing the formation of thin films [1]: (a) the layer-by-layer growth (Frankvander Merwe or FM mechanism); (b) a three-dimensional nucleation, forming, growth and coalescence of islands (Volnier-Weber or VW mechanism); and (c) adsorption of a monolayer and subsequent nucleation on top of this layer (Stranski-Krastanov or SK mechanism). Which mechanism actually dominates in the formation of a multilayer depends on the strength of interaction between the atoms of the growing film and between the atoms of the film and the substrate. Figure 1 illiustrates these three basic modes of initial nucleation in the film growth.

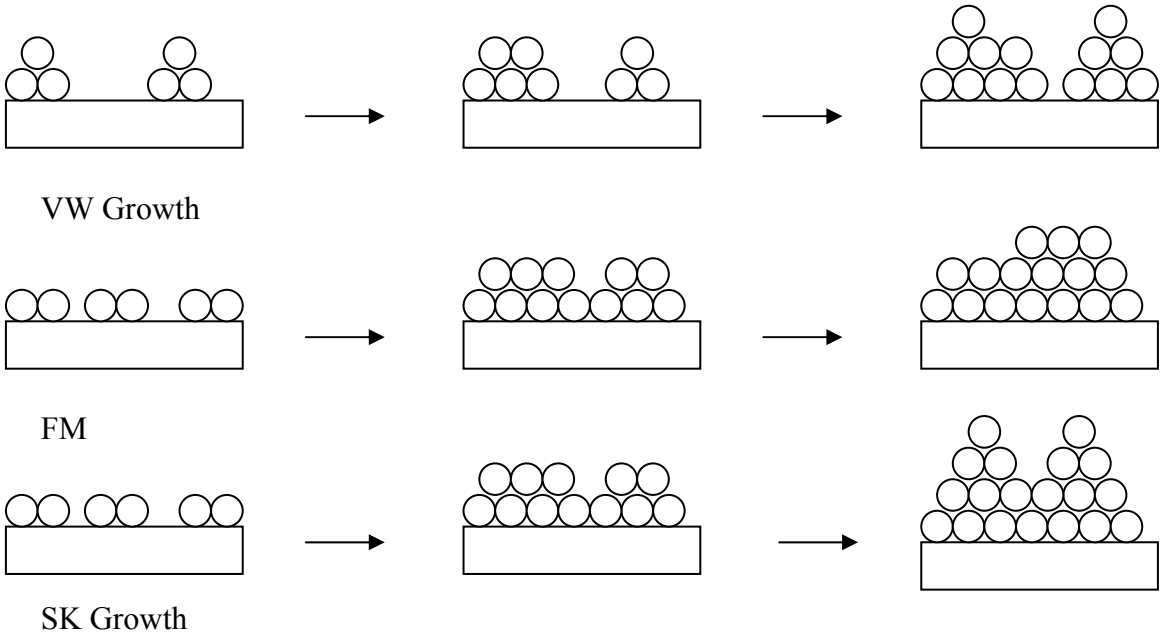

Fig. 1.1 Basic modes of initial nucleation in the thin film growth.

Simple energetic arguments are often used to predict the growth mechanisms of a superlattice [2]. The FM nucleation takes place if the surface energy is reduced when covering an A surface with B. The surface energy is defined as the reversible work done on a system by the external forces to create a unit surface area at constant temperature. In terms of W_A and W_B, the vacuum surface energies of A and B, respectively, and Wm, the energy of the A-B interface, FM nucleation of B on A results if

$$W_B + W_{AB} \leq W_A \quad (1.1)$$

When A is subsequently deposited on B, the condition for FM nucleation is:

$$W_A + W_{AB} \leq W_B \quad (1.2)$$

The most common case when both equation (1.1) and (1.2) are satisfied is when A and B have similar chemical and structural properties so that $W_{AB} \cong 0$ and $W_A \cong W_B$, as in Ag/Au multilayer. Another case in which both equations (1.1) and (1.2) can be satisfied is when A and B react strongly so that W_B is negative.

There are many material combinations for which equations (1.1) and (1.2) are not satisfied simultaneously. If A has a much higher surface energy than B, that is $W_A >> W_B$, layer A will nucleate as three-dimensional (3-D) islands and the VW mechanism takes place. Another common case is when A and B are much different either chemically or structurally so that W_{AB} is large and positive. Depending on the values of W_A and W_B, one or both layers will nucleate through the VW mechanism. The SK mechanism works when the structural and chemical differences between A and B are small. In this case, an intermediate nucleation mechanism is observed where 3-D islands form after one or more complete layers have been deposited.

The structural difference between two materials A and B can be represented by the lattice misfit (or mismatch) ε which is defined as:

$$\varepsilon = 2(d_A - d_B)/ (d_A + d_B) \quad (1.3)$$

Where d_A and d_B are the stress-free layer lattice spacings of materials A and B respectively. The multilayer mismatch ε plays an important role in determining the characteristics of the interfaces.

Multilayer with larger ε has less planar interfaces than those with smaller ε [2]. In most cases, there is a considerable lattice misfit ε between the two materials A and B and

therefore the VW mechanism takes effect. It has been found [l] that the growth of multilayer by the VW mechanism can be divided into the following three stages:

(a) Nucleation. Atoms of the depositing materials reach the substrate and are attracted to the surface by forces mostly of dipole or quadruple character. They become, at least for a certain time, adsorbed on the surface and become adatoms. These adatoms are statistically distributed over the substrate and form nuclei for further growth;

(b) By surface diffusion. Some adatoms become attached to the surface of the already existing nuclei and form individual islands, which often have the shape of small crystals (crystallites);

(c) Coalescence of the islands and formation of a more or less connected network containing empty channels. Coalescence may happen three ways: (1) Ostwald ripening: a larger nucleus grows by engulfing a smaller one close to it. This process is slow and it happens mostly in treatment after deposition.

(2) Coalescence due to mobility of islands: Smaller nuclei are more mobile than larger ones. They move and get absorbed by larger ones. This process is also too slow to play a significant role in deposition.

(3) Coalescence by growth: this is the most important one. If two growing particles touch each other, they can - depending on the substrate temperature and the surface energies - either agglomerate by retaining their shapes almost entirely or go through a liquid-like coalescence (at higher substrate temperatures or if the film is amorphous) process to form a single larger one.

1.2. Formation of the orientation of multilayer

Multilayer has a crystalline structure. The structure of a multilayer depends on its constituent materials, the deposition method, which determines the growth pattern of the thin film, the substrate on which it is deposited and some other factors. Crystals growing on a substrate may be variously oriented. The possible orientations are shown in Figure 1.2. Case (a) illustrates a completely disordered film, in which the directions of axes of individual crystallites are distributed randomly. Case (b) describes a state in which one particular axis of ail the crystallites is oriented in approximately the same direction. This

is called a fist-stage orientation or a single texture. Case (c) depicts the second-stage orientation or double texture. Finally, case (d) depicts a monocrystalline orientation, which is very important because it includes also the case of epitaxial films.

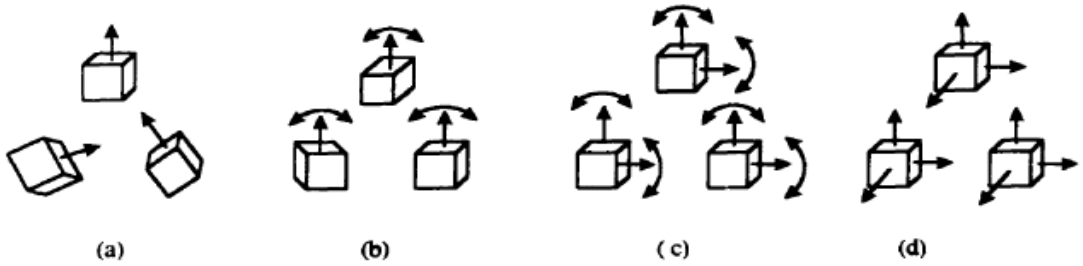

Figure 1.2: Orientation of crystallities on substrates. (a) chaotic ordering; (b) single fiber texture; (c) double texture; (d) monocrystalline orientation (double arrows indicates departures from prevailing orientation)

An important phenomenon in thin film growth is the epitaxial growth of a superlattice, that is, the formation of monocrystalline films on monocrystalline substrates either of the same substance or of another substance. The resulting orientation of the thinfilm depends on the crystal structure and orientation of the substrate. Epitaxy can occur between materials of different crystal structure and of different chemical bondings. Observation of film structure during their preparation reveals that epitaxy begins to take place in the nucleation stage, but the stages of growth and coalescence of islands can be decisive for the final structure of the film.

The nuclei growing on a substrate may initially have various crystallographic orientations. It has been established though that when two islands which are of different sizes and crystallographic orientations coalesce, the resultant crystallite assumes as a rule the orientation of the larger one. This means that the growth conditions will determine the final orientation of a multilayer, that is to say, the multilayer will eventually adopt the orientation of the nuclei that the growth conditions are most in favor of.

In some cases when the substrate has a lattice constant approaching that of the film (the difference between them being less than 0.2%*),* "pseudomorphism" occurs and the film assumes the structure of the substrate until a thickness of the order of 10 nm is reached. If

the difference is greater and the binding between the substrate and the film is strong, pseudomorphism occurs for only the earliest atomic layers. Still greater differences are accompanied by the formation of lattice defects (e-g., dislocations). An important variable defining superlattice structure is the strain state of the layers. This is represented by the superlattice misfit:

$$\varepsilon = \varepsilon_{coh} + \varepsilon_{dis} \tag{1.4}$$

Where ε_{coh} is the coherency strain and ε_{dis}, is the portion of the mismatch accommodated by dislocations. During the initial stages of depositing B on A, B is strained such that its lattice parameter matches that of A i.e., the A/B interface is coherent and is at its maximum. Upon further deposition, the interfacial coherency is lost by the introduction of interfacial misfit dislocations, which either partially or fully relax the lattice spacing of B to its stress free value. When B is completely relaxed, $\varepsilon_{coh} = 0$.

An estimate of the coherency strain ε_{coh} expected in a layer is given by [2]:

$$\varepsilon_{coh} = \left(\frac{D}{2Bh}\right)\ln\left[\left(\frac{h}{b}\right)+1\right] \tag{1.5}$$

In equation (1.5),

$$B = \frac{2G_f(1+\nu)}{(1-\nu)} \tag{1.6}$$

Where G, is the shear modulus of the film material, v is the Poisson's ratio which is related to the shear modulus G and elastic modulus Y by $Y = 2G(1+\nu)$, and

$$D = \frac{G_f G_s b}{\pi(G_f + G_s)(1-\nu)} \tag{1.7}$$

Where *G,* is shear modulus of the substrate. In deriving equation *(1.5)* it is assumed that the film thickness h < 2s, where $s = b/(\varepsilon - \varepsilon_{coh})$ is the separation between dislocations and b is the Burger's vector.

For small enough film thickness h, equation *(1.5)* gives $\varepsilon_{coh} > \varepsilon$. This is physically unacceptable, but rather implies that the film is strained to match the underlying material without misfit dislocations. As h increases, ε_{coh} will decrease until $\varepsilon_{coh} < \varepsilon$. A fraction $(\varepsilon - \varepsilon_{coh})/\varepsilon$ of the mismatch will then be accommodated by dislocations. Since ε_{coh}

continues to decrease as h increases, the film approaches complete relaxation with continued deposition. A critical thickness h_c, can be determined [2] using the condition $\varepsilon = \varepsilon_{coh}$:

$$h_c = \left(\frac{D}{2B\varepsilon}\right)\left[\ln\left(\frac{h_c}{b}\right)+1\right] \tag{1.8}$$

for single layer film, and

$$h_c = \frac{b(1-\nu\cos^2\psi)\left[\ln\left(\frac{h_c}{b}\right)+1\right]}{2\pi\varepsilon(1+\nu)\cos\varphi} \tag{1.9}$$

for multilayer films. Where, ψ is the angle between dislocation line and its Burgers vector and φ is the angle between the slip direction and the direction in the film plane that is perpendicular to the interface slip plane intersection.

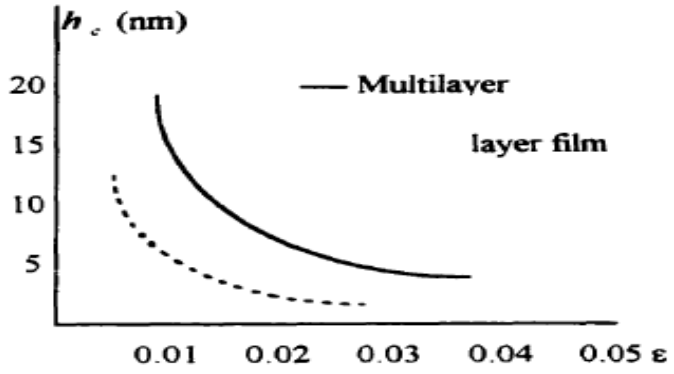

Figure 1.3: Dependence of critical thickness h, on multilayer misfit ε.

At thickness h_c it is energetically favorable for misfit dislocations to form. The dependence of h_c, on ε is shown in Figure (1.3) [2].critical thickness for multilayered films is larger than that for single layer film. This is because the strain is divided between the depositing layer and the underlying layers.

1.3. Crystallographic structure of copper and nickel

For the copper and nickel system studied in this work both constituent materials have the fcc structure.Their lattice constants d are 3.615 and 3.526 angstroms respectively with an

interface misfit ε of 2.5% for the {100} Cu and {100} Ni interplanar spacings. The mismatch value indicates that a VM mechanism will take place in the growth of the Cu/Ni multilayer, and on a copper substrate with prevailing {100} orientation, the multilayer will have a dominant {100} orientation. This is confirmed in the experimental part.

1.4. Electrodeposition

Electrodeposition or electroplating has been termed as the process in which the deposit of a (usually) thin layer (of metal) is formed 'electrolytically' on a substrate (that is usually a metal). The purpose of such process may be to enhance or change the substrate's appearance and/or attributes such as corrosion resistance. Examples include the deposition of gold or silver on jewelry and utensils, and the deposition of chrome on automobile parts. The object that is to be plated is submerged into the electrolyte (plating bath). Placed usually at the center of the bath, the object that is to be deposited acts as a negatively charged cathode. The positively charged anode completes the electric circuit; those may be at opposite edges of the plating tank, thus making the deposition possible both sides of the cathode. Material systems with nanostructures are developed with ease because of the processing being carried out at relatively low temperatures and some of the processing is carried out with a surfactant that retains the nano features. The key variables of the electrodeposition include temperature of the bath, current density complexing agents, agents to improve the bath conductivity and pH. These can be manipulated in achieving the required grain size in nanocrystalline range.

1.4.1. Fundamental equation for an electrochemical deposition:

Electrodeposition refers to the process of depositing a material (typically metal) from a solution (called electrolyte) on another one through an electrochemical reaction. It was first used to make multilayers in 1921 when Blum [3] deposited copper/nickel and other multilayered films by alternate deposition from two different electrolytes. This is called dual-bath deposition. Later, multilayers have been produced from a single electrolyte which contained two or more kinds of metal ions. This is called single-bath deposition. By getting rid of the trouble of mechanically switching the samples between two baths,

the single-bath method is simpler to implement and it allows multilayers with graded interfaces to be made by tailoring the deposition waveform. However, it is restricted to certain pairs of materials or composition ranges because of the requirement for a compatible electrolyte and the limited range of alloy compositions that can be deposited from a given electrolyte. Also, it is impossible to deposit a pure layer of the less noble metal (a less noble metal requires a more negative reduction potential) with a single bath. The most successful single-bath multilayer deposition technique is the one developed by Tench & White [4] and Yahaiom & Zadak[5]. The single-bath technique is preferred by most researchers and is the choice in this work. By controlling the compositions of the two materials in the electrolyte and the proper selection of deposition parameters, even the less noble material can achieve very high purity in the multilayers. An electrochemical reaction (or electrode reaction) involves not only molecules and ions, but also negative electrons e^- arising from a metal or other substance by metallic conduction. Such a reaction is called oxidation if it proceeds in the direction corresponding to the liberation of electrons; and it is called a reduction if it proceeds in the direction corresponding to the absorption of electrons. For example,

Oxidation: $Cu \rightarrow cu^{2-} + 2e^-$

Reduction: $Ni^{2-} + 2e^- \rightarrow Ni$

To understand how an electrochemical reaction occurs, it is helpful to start with the electrode reactions (electrode processes). If a metal electrode is immersed in a solvent (water in this work), some of the metal ions will be freed from the binding of their metal lattices due to collisions from the molecules of the solution and enter the solution. As the concentration of the metal ion in the solution increases, some ions will be re-absorbed and neutralized by the electrode surface and eventually an equilibrium state will be reached between these two processes. At this stage, the number of ions entering the solution equals the number of ions reabsorbed and neutralized at the electrode. After the ions leave the surface of the electrode, a layer of electrons will be accumulated at the electrode surface. These electrons then attract a layer of ions to them, forming an electrical double layer as shown in Figure 1.4. As a result, a potential difference is established between the electrode and the solution. In practice, this potential is characterized by the standard electrode potential U^0.

The simplest model of the structure of the metal solution interphase is the Helmholtz compact double layer model as shown in figure-1.4.According to this model ,all the excess charge on the solution side of the interphase ,q_s is lined up in the same plane at a fixed distance away from the electrode ,the Helmholtz plane (HP, Fig-1.4).The fixed distance X_{HP} is determined by the hydration sphere of the ions.it is defined as the plane of the centers of the hydrated ions .All excess charge on the metal q_m is located at he metal surface .Thus according to this model ,the interphase consists of two equal and opposite layers of charges ,one on the metal (q_m)and other on the solution (q_s).This pair of charged layers ,called double layer ,is equivalent to a parallel plate capacitor .the variation potential in the double layer with distance from the electrode are linear(fig-1.4)A parallel plate condenser has capacitance per unit area given by the equation

$$c = \frac{\varepsilon}{4\pi d} \qquad (1.10)$$

Where ε is the dielectric constant of the material (the dielectric) between the plates and d is the distance between the plates. For constant values of ε and d, the Helmholtz model predicts a potential independent capacitance. This is in contradiction with experiment .Thus the interphase does not behave as a simple double layer .There are various new advanced model like Gouy-Chapan diffuse charge model ,stern model and Grahame triple layer model .As per the Cu/Ni bath is concerned the formation of the multilayer by the Helmholtz model is the most prominent one for fomentation of the double layer . As stated previous the surface free energy for the formation of this double layer is much less than any other case of formation

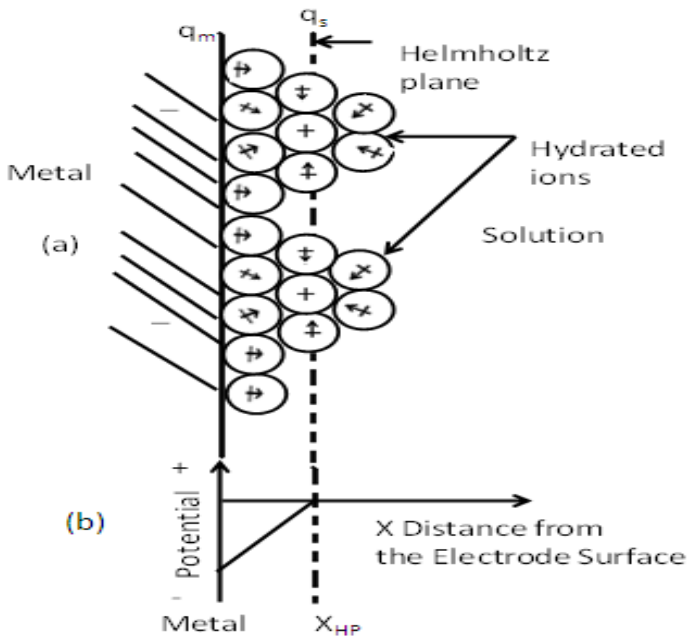

Figure1.4. (a) Helmholtz model of a double layer: qm.excess charge density on metal; q_s, excess charge density in solution, on HP ; (b) linear variation of potential in the double layer with distance from the electrode .

1.5. The electrochemical reactions in the Cu/Ni multilayer bath

From the standard electrode potentials table [6], we know that for the reaction

$$Cu^{2-}+2e^{-}= Cu \qquad (1.11)$$

the standard electrode potential is 0.3394V; and for the reaction

$$Ni^{2-} + 2e^{-} = Ni \qquad (1.12)$$

the standard electrode potential is -0.25V.

It should be noted that these potentials are the standard electrode potentials as defined above and are not the real potentials that should be used in the real experiments. However, they indicate that copper has a higher reduction potential (or less negative potential) than nickel, therefore we say copper is a more noble metal and nickel is a less noble metal. The reduction potentials for each of the two metals in a certain electrolyte can be experimentally determined using a voltammogram. A voltammogram is a diagram which shows the current dependence on the potential applied to an electrochemical cell as is shown in Figure 1.5. .

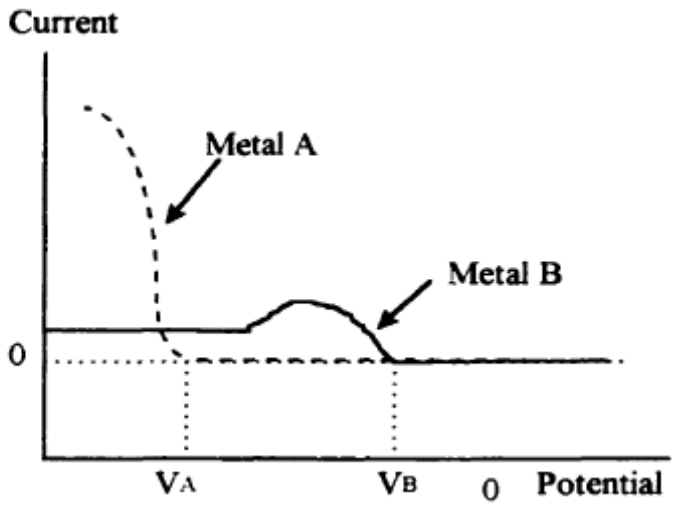

Figure 1.5: Schematic diagram showing the current dependence on potential for an electrolyte containing metal A and B with metal A having a much higher concentration than metal B.

Starting at potential V_B, reduction of metal B begins and a current can be detected at the cathode. From V_B down to the potential at V_A, only metal B is reduced. As the potential further decreases from V_A both metal B and metal A are reduced. The current increases sharply because metal B has a much higher concentration in the electrolyte. Theoretically, any potential value in the range of between V_B and V_A can be used to reduce metal B only; and any value lower than V_A can be used to deposit metal A with a certain impurity of metal B.

1.5.1 Advantages

- A room temperature processing technique that can be used both as a coating and free-form manufacturing technique.
- Process parameters can be controlled at will to achieve the end properties.
- An established industrial infrastructure (i.e., electroplating and electroforming industries),
- A relatively low cost of application where by nanomaterials can be produced by simple modification of bath chemistries and electrical parameters used in current plating and electroforming operations.

- The capability in a single-step process to produce metals, alloys, and metal-matrix composites in various forms (i.e., coatings, free-standing complex shapes), and most importantly.
- The ability to produce fully dense nanostructures free of extraneous porosity.

1.6. Sonoelectrochemical process

Electrochemical methods are of widely recognized importance in the generation of reactive intermediates and organic electrosynthesis can provide transformations to compounds which may be difficult to prepare by other means. Nevertheless, when laboratory electrolytic processes are scaled up for industrial exploitation, some restrictions appear such as limitation of mass transfer to the electrode surface (which equates to a limitation of reaction rate), fouling of the electrode surface and evolution of gases during the electrochemical reaction. Ultrasonic vibration, which can lead the collapse of cavitations bubbles to large pressure and thermal differentials on microscopic scale together with high energy intermediates formation and accelerated mass transport, should clearly improve electrochemical methodology. Ultrasonic waves could indeed continuously clean and activate the electrode surface, disturb the diffusion layer, decrease the depletion of electroactive species near the electrode surface and limit the accumulation of gas bubbles evolving at the electrode.

Chemical and physical effects in liquid media under the effect of powerful sonication are connected, primarily, with the phenomenon of ultrasound cavitation.It is well known that the process of ultrasound cavitations takes place when the amplitude of sound pressure P_a exceeds the threshold value P_m, the last being determined by the ultrasound frequency and directly correlating with it. Providing $P_a > P_m$ the cavitations cavity is increased to a definite volume followed with its collapse in a short period of time. Collapse is accompanied with significant energy release; the collapse of a bubble results in pressure of about 1800atm in the bubble itself and around it in the nearest liquid volume, the local temperature being increased to 5000 ^{0}K, and the rate of temperature change is 1010 ^{0}K . In our experiments $P_m < P_a$ for 20 kHz but in the case of 200 kHz, $P_m > P_a$. Thus the effect of using only high-frequency (200 kHz) ultrasound vibrations on the reaction medium is limited exclusively to vibration of the cathode surface where reduction of iron

ions takes place and cavitation in the liquid medium is out of the question. In case of only low-frequency (20 kHz) ultrasound a region of intensive cavitation is formed in the interelectrode space. Under the effect of micro shocks caused by cavitation collapse the particles which are deposited on the cathode surface are transferred into the electrolyte, wherein the cavitation effect is continued, so as to deposition start.

1.6.1 Advantages of sonoelectrochemical processes

- Causing extremely fast mass transport
- Enhancing the mixing and dissolutions kinetics at low temperature and
- Affecting the formation of solid at the electrode surface

1.7. Effect of interface between bilayer depositions

The role of interfaces in materials often plays a decisive part in determining physical properties. Three basic multilayered structures may exist, as shown in Fig 1.6.The role of interfaces affects the macroscopic characteristics such as mechanical, electronic, magnetic and thermodynamic properties.

This interest has been substantially increased by the continuing effort to push the size of phase in multiphase materials down to nanoscale dimensions [7]. There are three basic concepts in dealing with interfaces in nanoscale dimensions. The first is related to the coherency of atoms across the interface The nature of the interface itself, however, as it relates to smoothness, flatness, the amount of disorder and interdiffusion, is of fundamental interest to any interfacial property And, when interfaces are apart by a few interplanar spacings, interference effects have a profound effect on equilibrium structure. The order/disorder state of the interfacial structure, induced during the composition modulated synthesis, becomes increasingly property significant as the multilayer period decreases, *i.e.* the proportional number of interfaces increases.

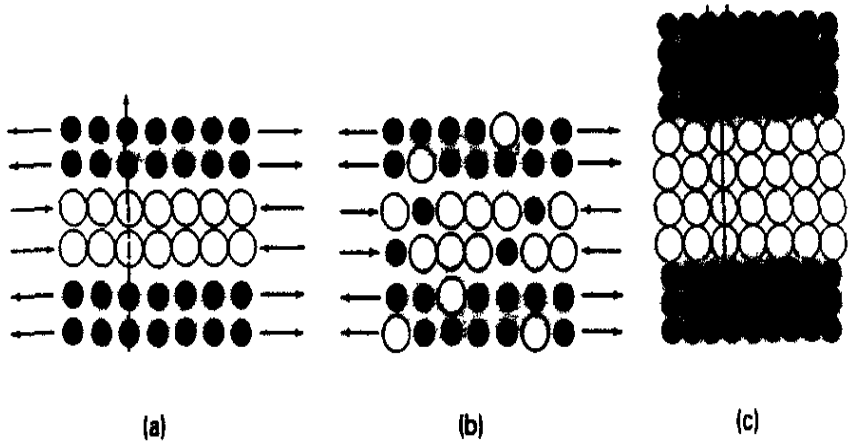

Fig 1.6 Multilayered structures (a) coherent superlattice, (b)composition-modulated alloys, in which coherency is maintained but interdiffusion has taken place during deposition of subsequent annealing, (c) incoherent-modulated structure, in which misfit dislocations appear at the interface.

The presence or lack of interlayer coherency is dependent on the atomic misfit between host lattices compounded with short-long-range interactions, as well as the deposition-dependent growth morphology.

The origin of the GMR effect is believed to be the interfacial spin-dependent scattering of electrons as they traverse through a thin non-magnetic layer between two magnetic layers. This scattering and, hence, the magnetoresistance is enhanced when the magnetization of adjacent magnetic layers is in opposite directions i.e. antiparallel configuration and minimized when the magnetizations are in the same direction parallel configuration., which means that an antiferromagnetic coupling is required in order to arrive at 'giant' values of the magnetoresistance. It is observed, however, that the properties of multilayer structures are critically dependent on the growth conditions. It has been demonstrated for example, in the case of the Ni–Cu system, that very perfect thin Ni/Cu multilayers can be prepared with coherent interfaces if the layer modulation wavelength is in the 10-nm range; at modulation thicknesses above about 60 nm, the interfaces lose their nearly perfect coherency.

1.8. Effect of low temperature on multilayer deposition

The solution temperature is clearly one of the most important factors controlling the surface morphology. High solution temperature generally produces higher surface irregularities. Electrolytic silver films, which have a low melting point temperature,

become large-grained with increasing solution temperature. An increase in the grain size with increasing solution temperature is closely related to the improved supply rate of metal ions, the increased diffusion distance of cations, and the increased surface diffusion distance of adatoms. It can be easily seen that the increased diffusivity allows adatoms to migrate a long distance over the substrate surface, thus producing large grains. So lowering the temperature we can approach towards the nano grain size.

Table 1 depicts the material systems that have been electrodeposited and the property amelioration that resulted as a consequence.

1.9. Properties Amplification

1.9.1. Mechanical properties

It is widely accepted that ultrasonic agitation increases the hardness of electrodeposited metals, although there exists some divergence of view regarding the magnitude of the increase obtained and the factors responsible. For example, Mtiller and Kusslg found that the hardness of chromium deposits produced on a vibrating cathode (f =16 kHz) increased by an average of 40%, whereas the hardness of copper, nickel and chromium deposits obtained in an ultrasonic field (f = 320 kHz) increased by only 15 to 20%. Other peoples also observed that electrodeposits produced in an ultrasonic field were harder than deposits obtained by conventional practice [8]. In all cases the hardness of the deposits formed under ultrasonic conditions exceeded that of deposits from an electrolyte subjected to air agitation; silver was only 15% harder, copper 48%, whereas the increase was much higher for cadmium (160%) and zinc (106%).

Similarly Kochergin and Vyaseleva [9] reported that the hardness of nickel deposits formed in an ultrasonic field (f = 23 kHz, Z = 2 x 104 Wm^{-2}) were 60% harder than those produced under ordinary conditions.

Table 1.1

Material	Property amelioration
Ni-based alloys	High solid solubility, negligible localized corrosion, coefficient of friction, wear resistance , strength, hardness, electrical conductivity[8]
WC/Co Ni, WC/Co Ni P	Wear resistance [9]
Ni–ZrO2	Hardness improvement[10]
Ni–TiO2	Improved hardness and corrosion resistance [11]
Ni–alumina	Low coercivity [12]
Ni–Co/Si3N4	High hardness, wear resistance [13]
CoNiCu/Cu and Co/Cu	SNMS depth profile analysis [14]
Ni from sulphate solution	Effect of Cr^{3+} on the electrodeposition and surface morphology study [15]
Cu/Ni	Influence of brighteners on friction and wear of electrodeposited multilayer films[16]
Ni-Co-Cu/Cu	Calculation element distribution and experimental depth profile analysis [17]
Ni/Cu	Effect of Ni sublayer thickness on sliding wear characteristics [18]
CoNiP	Effect of solution composition, solution pH and film thickness on the magnetic properties, phase and microstructure [19]
Ni/Cu	Study of microstructure of the multilayer from citrate bath [20]
Cu-Ni-P	Surface morphology studied ,depth profile analysis using TEM analysis [21]
Cu/Co	Electrochemical and physical properties of the multilayer [22]
Co/Cu	Microstructure Modification [23]
Co/Cu	Synchrotron X-ray reflectivity study of multilayer

	[24]
Co/Cu	Characterization by SEM,TEM,XRD and magnetoresistance study [25]
CO/Cu	Magnetic properties studied by VSM and SQUID [26]
Co/Cu	Interfacial roughness and magnetoresistance [27]
Cu/Co-Cu	Influence of a superimposed magnetic field and of annealing conditions on the microstructure and grain growth by ECSTM. [28]

Several workers [12] have found that the hardness of chromium deposits increased by approximately 100% when obtained at current densities of up to 20,000 Am^{-2} from a chromate electrolyte subjected to ultrasonic agitation (J= 19.5 kHz, Z = 0.8-1.25 x 104 $Wm^{-2)}$ Walker and co-workers [14, 15] found that the hardness increased with the application of ultrasound (f = 30 kHz) in several metal deposits. Copper deposits from the acid sulphate bath became harder compared with the still bath, 75 to 111 HV[18] and 86 to 105 HV[10] depending upon the conditions, while those from the cyanide bath changed from 146 to 185 HV[13]. The hardness of nickel deposits from the Watts bath increased25 from 241 to 310 HV and 215 to 242 HV but the change in zinc was negligible (46 to 49 HV). It was observed that the hardness of copper deposits from the sulphate bath, both with and without the addition of a brightening agent, benzotriazole, increased with a rise in the current density from 50 to 650 Am^{-2}; the effect of ultrasound was larger at the higher current densities. There are a number of exceptions to the general finding that ultrasound increases the hardness of electrodeposits. The hardness of nickel coatings obtained from sulphate electrolytes at various current densities in the range of 100 to 200 Am^{-2} was studied [29], who found that ultrasound (f = 30 kHz, Z = 3 x 103 Wm^{-2}) reduced the hardness of nickel deposits by approximately100 HV. Since a smaller grain size was observed, the fall in microhardness was explained by a reduction in the degree to which atomic hydrogen penetrated the nickel lattice during electrodeposition.

Transition-metal nitride thin films with B1-structure group- IVB (such as TiN, ZrN) or VB (such as VN, NbN) are a technologically important class of materials due to their mechanical properties as well as chemical inertness. Multilayered systems consisting of

alternating nanoscale nitride layers have shown interesting hardness enhancement (reaching up to 100%) compared with monolithic films when bilayer period reduces down to a few nanometers. Since the early work of in the mid 1980s, much research activity has been focused on the search and design of superhard (hardness 40GPa) coatings (and on the basic understanding of small-scale plastic deformation mechanisms. Metal/ceramic superlattices have been investigated because these systems exhibit improved toughness and higher-temperature stability compared to nitride/nitride systems, while retaining a relatively high hardness (20–30 GPa). Sublayer thickness was investigated, as shown in Fig. 1.7. It can be seen that the nickel single-layer film had the lowest microhardness (HV 527). The multilayer with the ratio of 2:1 for sublayer layer thickness had the highest microhardness (HV 660). From the above results, it can be concluded that the multilayer with a low wear rate had high microhardness. The improved microhardness of the multilayer was due to the flowing stress of multilayers which was dependent on the thickness of the sublayer. The decrease in the thickness of the sublayer could increase the flow stress. In addition, the interface area between copper and nickel sublayers, which had much dislocation and defect, had a great strengthening effect on microhardness.

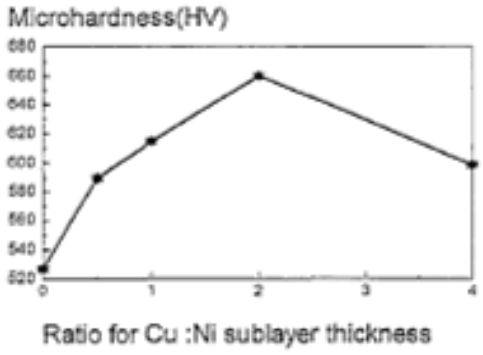

Figure-1.7.Microhardness of multilayers studied Vs.the different ratios for copper and nickel sublayer thickness [24]

However, the reason why the multilayer with the ratio of 2:1 for sublayer thickness of copper and nickel had the highest microhardness and the lowest wear rate rather than the multilayer with the ratio of 1:1 for Cu/Ni sublayer thickness could not be explained. It

may be dependent on the microstructure and physical properties of the constituent elements of metal multilayer.

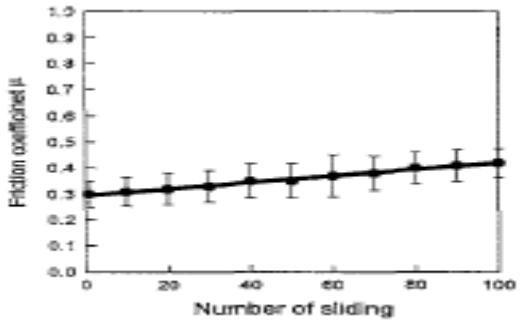

Figure- 1.8. Friction coefficient vs. the number of sliding of Cu/Ni multilayers with a sublayer thickness of 120 nm.[24]

Fig. 1.8 shows the friction coefficient vs. the number of sliding for Cu/Ni multilayers with a sublayer thickness of 120 nm. The friction test showed that the friction coefficient of the multilayers was not obviously changed when the thickness of the sublayer decreased. The friction coefficient of the multilayers was about 0.3-0.4. To understand the sliding wear characteristics of electrodeposited multilayers, sliding wear measurements have been conducted. Fig. 1.9 shows the curves of wear rates of the multilayers versus the ratios of copper and nickel thickness. It can be seen that the wear rate of the multilayers changed with different ratios for sublayer thickness of copper and nickel. The nickel single-layer film had the highest wear rate at 1.8 X 10^{-3} mm^3/N.m. However, there was the lowest wear rate of 3.45×10^{-4} mm^3/N.m when the ratio of copper and nickel sublayer thickness was 2:1.

It is well known that grain size has a strong effect on the ductility and toughness of conventional grain size (100mm) materials. On a very basic level, mechanical failure, which limits ductility, is an interplay or competition between dislocations and cracks. Nucleation and propagation of cracks can be used as the explanation for the fracture stress dependence on grain size.

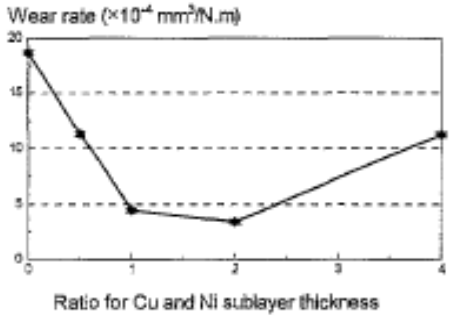

Figure-1.9.Wear rate of multilayers studied vs. the different ratios for copper and nickel sublayer thickness[24]

Grain size refinement can make crack propagation more difficult and therefore, in conventional grain size materials increase the apparent fracture toughness. However, the large increases in yield stress (hardness) observed in nanocrystalline materials suggest that fracture stress can be lower than yield stress and therefore result in reduced ductility. The results of ductility measurements on nanocrystalline metals are mixed and are sensitive to flaws and porosity, surface finish, and method of testing (e.g., tension or compression testing). In tension, for grain sizes < 30nm, essentially brittle behavior has been observed for pure nanocrystalline metals that exhibit significant ductility when the grain size is conventional. In some metals, Cu for example, application of ultra sound reduce the grain size, reduces the flaws and porosity inside the grains to almost 60% so that the ductile behavior is observed in compression, along with yield strengths about twice those observed in tension. While it is likely that the flaws and porosity present in many nanocrystalline samples seriously affect the results of mechanical tests and may be partly responsible for the asymmetry of results in compression compared to tension tests, the nature of the deformation process in terms of shear banding may also be important. The above behavior is presumably due to the inability of usual dislocation generation and motion to occur at the smallest nanocrystalline grain sizes.

1.9.2. Magnetic Properties

Giant magneto-resistive property

The main emerging technology for the recording head is giant magneto-resistive (GMR) technology, which was unknown until 1988.The primary advantage of the GMR head is

greater sensitivity to the magnetic field generated by the recorded bit on the disk. The increased sensitivity makes it possible to detect smaller recorded bits and read those at higher data rates. In the GMR head, resistance changes occur in the thin magnetic films separated by a thin conductor. One film has a variable magnetic orientation and is influenced by the disk's magnetic field; the second film has a fixed or pinned orientation. The GMR effect is based on the exchange coupling between a multiplicity of thin films of a ferromagnetic material (Fe) separated by thin films of a nonmagnetic material (Cr). The GMR phenomenon is believed to depend principally on the selective scattering of conduction electrons at the interfaces between the ferromagnetic and nonmagnetic layers. When an electrical field is applied, the spin-oriented conduction electrons accelerate until they hit a scattering center. The average distance the conduction electron accelerates is called the coherence length and it is of the order of ten nanometers in the metals used in the GMR superlattices. If the interlayer thickness is less than the coherence length, the conduction electron arrives at the interface of the adjacent ferromagnetic film still carrying its original spin orientation. When the adjacent magnetic layers are magnetized in a parallel manner, the arriving conduction electron has a high probability of entering the adjacent layer with negligible scattering, because its spin orientation matches with the layer's majority spins. On the contrary, when the adjacent magnetic layers are magnetized in an antiparallel manner, the majority of the spin-oriented electrons suffer from strong scattering at the interface because they do not match the majority spin orientation. When the magnetic layers are in the ferro state (magnetized parallel) the resistance is low and vice versa in the antiferro state. In the GMR structure, materials used in the interfacial structure must be immiscible and the interlayer must be thinner than the conduction electron coherence length. The GMR coefficient is strongly influenced by the domian structure, layer thickness, and atomic and mechanical defects in the GMR layers. Most advance use of multilayer structure of a GMR head consistes of a multilayer sandwich of CoFe and Cu with a pinned layer (FeMn, NiMn, PtMN, PdPtMn, IrMn, or NiO) at the top.

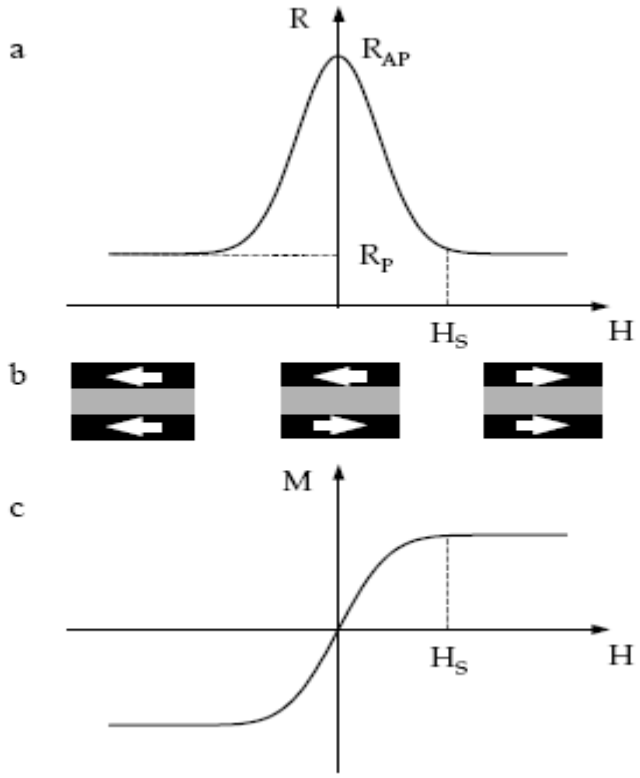

Figure-1.10 Schematic representation of the GMR effect. (a): Change in the resistance of the magnetic multilayer as a function of applied magnetic field. (b): The magnetization configurations (indicated by the arrows) of the multilayer (trilayer) at various magnetic fields: the magnetizations are aligned antiparallel at zero field; the magnetizations are aligned parallel when the external magnetic field *H* is larger than the saturation field H_S. (c): The magnetization curve for the multilayer.[25]

The GMR coefficient of a multilayer structure depends on the thickness of conducting Cu layer and number of the bilayers. Symmetric (or dual) GMR structures offer the possibility of achieving large GMR coefficients in the layers which exhibits relatively low saturation fields. In conventional spin valves, the pinning film of FeMn acts by providing an exchange bias whereas the NiO acts by inducing a very large coercivity in the adjacent Co film. In the bottom spin valve, the top Co film is unpinned and is free to switch magnetically at relatively low fields. In symmetric spin valve the top and bottom Co films are pinned and the central Co film is free. The symmetric spin valve structure exhibits higher GMR coefficient of 23.4% as compared to that of bottom structure (17%). The GMR coefficient is significantly increased by reducing the thickness of Cu layer in

the symmetric spin valve structure. The impediment of thinner Cu film is that the ferromagnetic coupling of the central Co film to the top and bottom Co film rises very sharply for Cu thickness lass than about 1.8 nm.

It was discovered that the application of a magnetic field to a Fe/Cr multilayer resulted in a significant reduction of the electrical resistance of the multilayer.

1. This effect was found to be much larger than either ordinary or anisotropic magnetoresistance and was, therefore, called “giant magnetoresistance” or GMR. A similar, though diminished effect was simultaneously discovered in Fe/Cr/Fe trilayers

2. As was shown later, high magnetoresistance values can also be obtained in other magnetic multilayers, such as Co/Cu. The change in the resistance of the multilayer arises when the applied field aligns the magnetic moments of the successive ferromagnetic layers, as is illustrated schematically in Fig-1.10. In the absence of the magnetic field the magnetizations of the ferromagnetic layers are antiparallel. Applying the magnetic field, this aligns the magnetic moments and saturates the magnetization of the multilayer, leads to a drop in the electrical resistance of the multilayer.

CHAPTER – 2

Materials & Methods

2. Materials and Methods

2.1. Methods

2.1.1. Electrodeposition

To alternatively deposit metal A and B, a potential waveform as show in Figure 1.9 can be applied. In electrochemical terminology the above mentioned method is known as chronoamperometry methods.

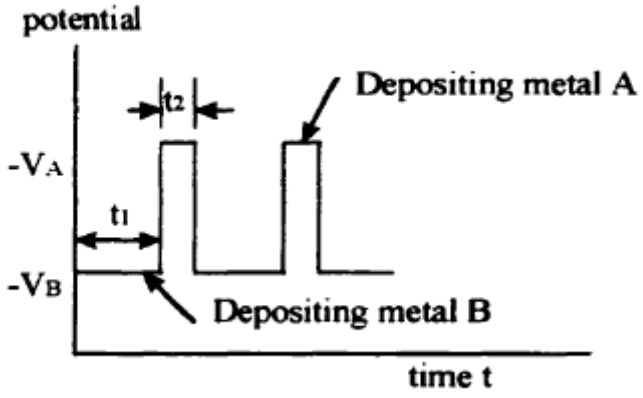

Figure-2.1: Potential waveform for the alternating deposition of metal A and B (not in scale).

As is shown in Figure 2.1, at less negative over-potentials, only the more noble metal B can be reduced and as a result a pure layer of metal B can be obtained during the deposition period t_1 shown in Figure 2.1. At more negative over-potential during deposition period t_2, both metal A and B are reduced and as a result an alloy of the two metals is obtained. This is one of the major drawbacks in the deposition of multilayer using a single-bath. It is impossible to obtain a pure layer of the less noble metal. However, if the ratio between the concentrations of metal B and A in the electrolyte is made large enough, the purity of metal B in the alloy layer can be made as high as desired. There is, of course, a trade-off in the requirement for deposition time. Lower concentration in metal B requires longer deposition time to obtain a certain thickness of metal B.

Thickness control

The time needed to deposit a certain thickness of a metal can be calculated using Faraday's Law. Faraday's law states that "in electrolysis, 96,500 Coulombs of electric charge produce chemical charge of 1 *g* equivalent." Let's consider a reduction reaction of metal M:

$$M^{n-} + n(e^-) \rightarrow M \qquad (2.1)$$

If the desired thickness is d (in cm) and the sample has a square shape with a radius r (in cm), the mass m (g) of the metal required to be deposited from the electrolyte is given by:

$$m = a^2 d\rho \qquad (2.2)$$

Where ρ is the density of material M in the unit of g/cm^3. The gram equivalent mg of this mass is:

$$m_g = \frac{m}{m_a} = \frac{a^2 d\rho}{m_a} \qquad (2.3)$$

where m_a, is the atomic mass of material M.

From reaction (2.1), we know that to produce 1 gram equivalent of material M, we need n gram equivalent of electrons. The total electrons m_{eg}, (in gram equivalent) needed to produce m_g, gram equivalent of material M is therefore:

$$m_{eg} = nm_g = na^2 d\rho / m_a \qquad (2.4)$$

From Faraday's Law, the total charges Q (in Coulomb) needed to produce m_{eg} gram equivalent of electrons is:

$$Q = \frac{Fna^2 d\rho}{m_a} \tag{2.5}$$

Where F = 96.500 is Faraday's constant.

Suppose the current during the deposition of metal M is I and is kept constant (this is a reasonable assumption for most experiments), the charges passed during time t (in second) is:

$$Q = It \tag{2.6}$$

Combining equation (2.5) with equation (2.6) gives:

$$t = \frac{nFa^2 d\rho}{m_a I} \tag{2.7}$$

This is the time required to deposit metal M with a thickness of d and a square sample of side a. It is in inverse proportion to current I. As I is in direct proportion with the concentration of metal M in the electrolyte, I is therefore in inverse proportion to the concentration. In a typical Cu/Ni multilayer deposition bath, the ratio of concentrations between Cu and Ni is about 1: 100 and accordingly the deposition currents for the two metals also have a ratio of around 1: 100. Therefore, to deposit the same thickness of the two metals, the time needed for Cu is about 100 times that for Ni.

The purity of the Ni layer can be estimated using equation (2.6). The mass deposited during time t is obtained by rewriting equation (2.7):

$$m = a^2 d\rho = \frac{tm_a I}{nF} \tag{2.8}$$

For the Cu and Ni reductions represented by equation (2.1) and (2.2), the masses for Ni and Cu deposited during time t are given respectively by equation (2.9) and (2.10):

$$m_{Ni} = \frac{tm_{aNi} I_{Ni}}{2F} \tag{2.9}$$

$$m_{Cu} = \frac{tm_{aCu} I_{Cu}}{2F} \tag{2.10}$$

Therefore the purity of Ni is expressed as:

$$p_{Ni} = \frac{m_{Ni}}{m_{Ni} + m_{Cu}} = \frac{m_{aNi} I_{Ni}}{m_{aNi} I_{Ni} + m_{aCu} I_{Cu}} \tag{2.11}$$

For a bath with a current ratio of 1: 100 between Cu and Ni, equation (2.11) gives a purity estimate of 98.9% for the nickel layer. In most experiments, the current ratio is even smaller and therefore the purity of the Ni layer is even higher than this estimate.

2.1.2. X-Ray crystallography

As a non-destructive testing technique, x-ray diffraction is a powerful tool for the analysis of crystalline structure. X-ray has wavelengths [30] comparable to the crystalline lattice constants, thus it can be used for the accurate measurement of crystalline parameters. Theories have been developed for x-ray diffraction in multilayer. Interpretation of x ray diffraction patterns from multilayer provides most of the important information about the structural characteristics of multilayer.

Bragg's law

If an x-ray beam is incident on a crystal surface, the x-ray beam will be scattered by the atoms on the crystalline lattice as is shown in Figure 2.2.

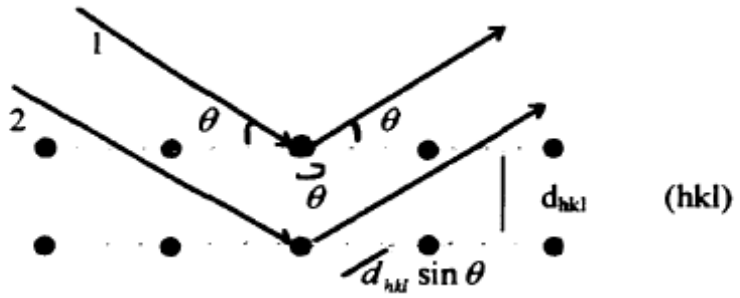

Figure 2.2: Scattering of X-ray by atoms on a crystal lattice

If the inter-planar spacing d_{hkl} and the incident angle θ satisfy the following equation:

$$2d_{hkl} \sin\theta = n\,\lambda \qquad (2.12)$$

Where λ is the wavelength of the X-ray beam and n is an integer, the scattered beam will be reinforced and a maximum of diffraction will be detected. Equation (2.12) is called Bragg's law. It can be explained as follows:

The difference in the distances traveled by ray 1 and ray 2 is $2d_{hkl} \sin\theta$ as indicated in Figure 2.2. If this difference is an integral multiple of the X-ray wavelength, the two rays will interfere constructively.

The Bragg's law requires that a λ and θ be matched by equation (2.12): x-rays of wavelength incident on a crystal at arbitrary angle will in general not be reflected. To satisfy the Bragg's law, it is necessary to scan a wide range of either the angle or the wavelength. Experimentally, it is usually the angle that is scanned while the wavelength is kept fixed. As a result, different groups of atomic planes with different Miller indices will be brought into position for reflection and a diffraction spectrum.

X-Ray diffraction patterns were recorded from 40˚ to 80˚ with a Philips X-pert MPD system diffractometer using Cu K_α with an accelerating voltage of 40 KV. Data were collected with a counting rate of 1˚/min. The K_α doublets were well resolved.

2.1.3. Texture determination

Texture or preferred orientation describes a preferred orientation, describes preferential alignment of the crystalline lattice of various grains in a polycrystalline aggregate. Texture does not define the shape of the grains; therefore, the presence or absence of texture cannot be inferred from the grains. For example, nonequiaxed grain shape is not a crystallographic texture, although the same process that develops a crystallographic texture in a metal may currently develop nonequiaxed grain shape. In general, crystals are anisotropic with respect to the properties; therefore control over texture is important because it provides a means for optimizing desired properties in a given direction in a polycrystalline metal.

The desirability of the texture control depends on the desired properties, the direction in which these properties are optimum and the direction of intend use for any given engineered material or alloy. Brittle materials cannot be deformed, and therefore the desired texture must be developed by casting powder metallurgy technique or

electrodeposition .Because physical and mechanical properties such as young's modulus and magneticflux density are affected by crystal direction, texture can be investigated by measuring these properties. However, although the dependence of a property on direction often can be calculated if the texture is known but the reverse is not true.

2.1.3.1 Pole figure techniques:

A pole figure technique is a stereographic projection that shows the distribution of poles, or plane normal, of specific crystalline plane using specimen axes as the reference axes .These techniques are widely used for examining sheet texture .for example, in examining a sheet specimen, all directions in the plane of the sheet (rolling plane) are projected as points inside the circumference of the pole figure circle.

Te rolling direction is always at the top of the ,and the transverse direction is usually designed at the right of pole figure .the centre of the circle corresponds to the direction normal to the plane of the sheet (normal direction).direction lying at angles between the normal direction and rolling direction plane project as points inside the circle. As simple illustration, consider a unit cell of single grain orientation in the sheet so that the (100) plane is parallel to the plane of the sheet and so that the two cube directions, respectively .this is illustrated by the position of the unit cell in figure 2.3(a). The pole figure of the cube planes, which can be projected in the pole figure are marked by arrows 1to5.

Data are conveniently gathered with commercially available automatic pole figure goniometer with the diffraction angle fixed at the desired pole position ,pole figure goniometer rotates the specimen to bring all the specimen orientation to the diffracting position .Data are obtained by determining the diffraction line intensity of poles as a function of specimen orientations. The measure d intensities can then be plotted as contour lines. From the position of the intensity maximums, so called ideal texture are often derived.

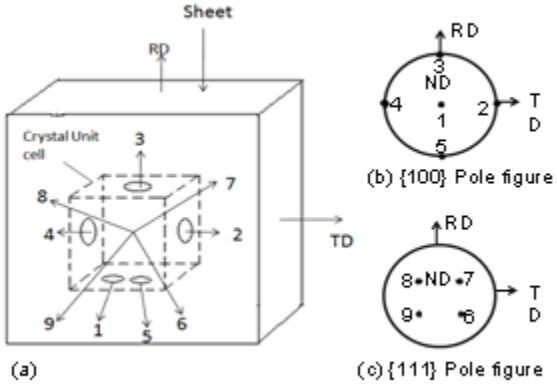

Figure-2.3.Schematic of pole figure representation of crystal orientation .In(a) a crystal unit cell is aligned as shown.(b) and (care pole figures showing positions of poles in (c),represented by arrows emanating from the centre of the unit cell .RD ,rolling direction ;TD, transverse direction ; ND ,normal direction.[31]

A {100} pole figure, showing the positions of these poles, is illustrated in figure 2.3(b). The pole of the same crystal are marked by arrows 6to9.the {111}pole figures then appears different only because poles of different planes are used .A pole figure is always specified by Miller indices of the poles.

Pole figure construction by point plotting, as illustrated by figure---is useful for coarse grained specimens, in which the orientation of each grain can be determined by Laue photography. For fine grained materials, the intensity data usually are represented as contour of equal value .Generally, the intensity value measured for a texture specimen to the value for a randomly oriented specimen.

2.1.3.2 Orientation distribution function:

The orientation distribution function is a more quantitative description of texture beyond the idealized orientation of the pole figures. This technique expresses the probability of a crystallite having an orientation described the Euler angles that relates the specimen axes with the crystal axes. (Fig-2.4). This function can be expressed by a series of expansions in spherical harmonics. The coefficients of this series can be obtained from the pole figure distribution obtained from the pole figure, which is similarly expanded in a series of spherical harmonics. Greater precision is obtained using data from several pole figures.

The orientation distribution function can be plotted in two dimensional sections using two of Euler angles as shown in figure 2.5.

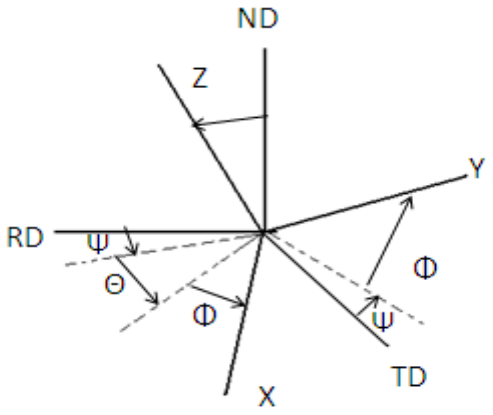

Fig-2.4.Euler angles Ψ,Θ,Φ relating to the specimen axes ,RD(rolling direction),TD (transverse direction),ND(normal direction),with the crystal axes ,x, y, z.[31]

However its usefulness lies in the quantitative comparison with the anisotropic properties of a texture specimen, such as Young's modulus, yield strength and magentocrystalline anisotropy energy. In these cases the orientation dependences of a given property in a polycrystalline sample is often expressed in terms of the coefficient of the series development of the crystallite orientation distribution.

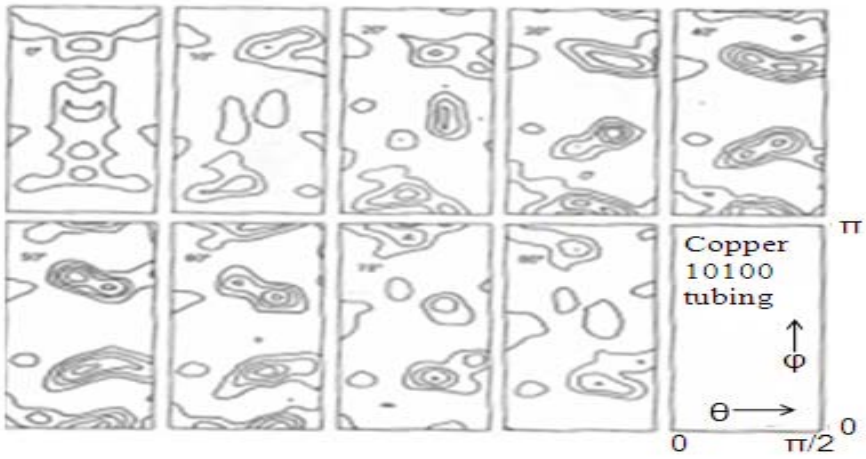

Figure- 2.5: The crystallite orientation distribution function .Numbers indicate the orientation points per unit volume.[31]

The factors affecting the texture of plated films were found to be: (1) the crystal system (the type of a metal), (2) the type of metallic salts (anions), (3) the current density (overpotential), (4) the film thickness, (5) the type of a buffer, (6) additives such as brighteners; and (7) a cation originating from a reagent added as the supporting electrolyte. Figure 2.6(a)-(d) describe a change in the texture index of electrolytic copper films obtained from a pyrophosphate bath as a function of film thickness [32] at the current densities of 100, 300, 500, and 1000 A/m^2, respectively (Watanabe et al., to be submitted). All the thin copper films show the <111> texture for all current densities. The copper films obtained at low current densities also maintain the 111 texture, even with increasing current densities and film thickness.

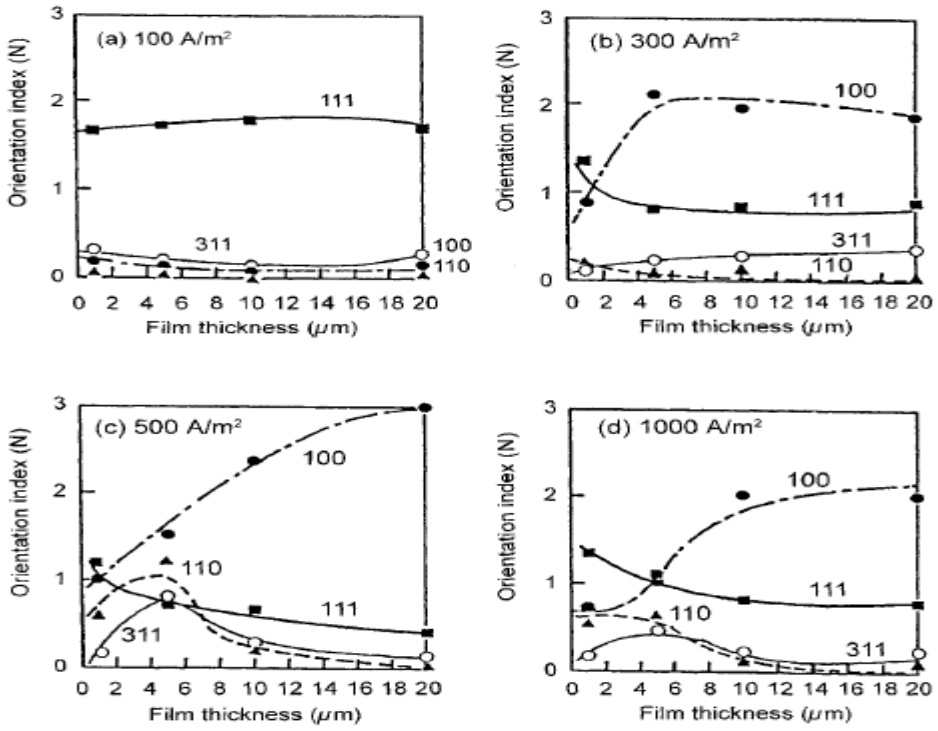

Figure-2.6. A texture change with increasing film thickness and current density in electrolytic copper films grown on amorphous alloy substrates from a pyrophosphate bath. The solution temperature is 55 °C and pH is 8.7[32].

As the current density exceeds 300 A/m^2, the texture changes to the 100 texture with increasing film thickness. Figure-2.7 shows the texture index for electrolytic copper films

(obtained at two current densities (500 and 1000 A/m^2) from a sulfate bath) plotted against film thickness. At low current densities, the films are seen to display the 110 texture. At high current density, no texture was initially present but the 110 texture developed with increasing film thickness. The texture of plated films thus changes with the current density and the type of a bath (the type of anions present).

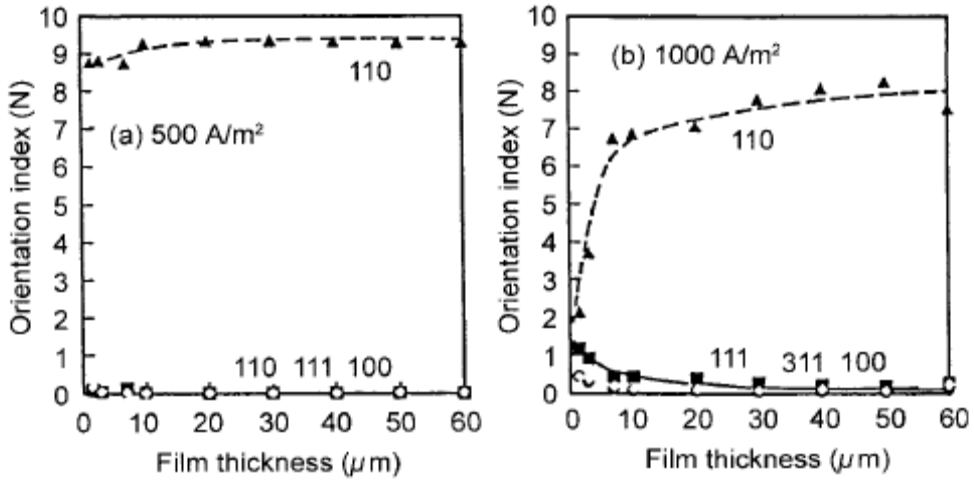

Figure-2.7. A texture change with increasing film thickness in electrolytic copper films grown on amorphous alloy substrates at the current densities of (a) 500 and (b) 1000 A/*m*^{2} from a sulfate bath. The solution temperature is 60 °C and pH is 2.0[32].

X-Ray diffraction patterns were recorded from 40˚ to 80˚ with a Philips X-pert MPD system diffractometer using Cu K_α with an accelerating voltage of 55 KV. The samples analyzed were, nickel on top and copper on top. The angle was adjusted so that the penetration depth of X ray will be below 1000 nm to record the solely the deposit values rather the substrate values.

2.1.4. Nanoindentation for hardness characteristics

Hardness is a measure of a material's resistance to plastic deformation caused by surface indentation or abrasion. It is usually measured by pressing a diamond tip of a specially-designed shape into the surface of a sample. The hardness is then characterized by the size and shape of the indentation. It is defined to be the force F divided by the indent area

S, that is, H = F/S. Hardness is typically expressed in unit of Gigapascals (1 GPa = 10^6 N/m^2) .There are a number of ways in hardness measurement, each of them using a different indentation tip and a different range of force applied. The interpretation of the indentation area is key to determining the precision of the hardness measurement.

When a material is subject to an external force, its mechanical structure will undergo a series of changes depending on the magnitude of the force applied. This process can be illustrated by the stress-strain curve as show in Figure 2.8.In Figure 2.8, the region from the origin to point p is the elastic deformation area in which the strain and stress are proportional and the deformation will vanish once the applied force is removed.

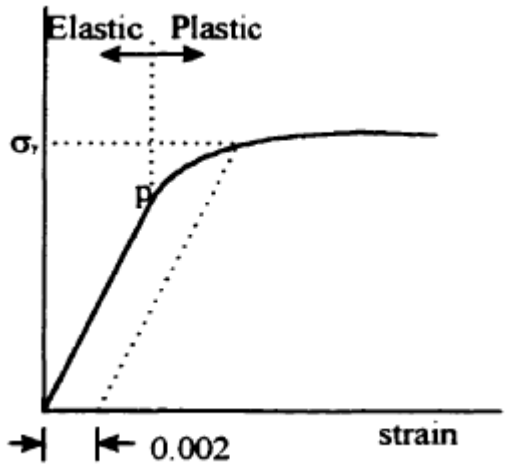

Figure- 2.8: Stress-strain curve of a material

.The strain ε and stress σ are related to each other according to Hooke's Law:

$$\sigma = Y\varepsilon \qquad (2.13)$$

Where Y is the elastic constant of the material.

Passing point p, the strain is no longer in proportion with the stress and the deformation becomes non-recoverable and permanent. This is the plastic deformation area. For most metallic materials, plastic deformation occurs at strain values around 0.005. In materials engineering, it is important to know at which stress level plastic deformation begins, that is the stress level at which the phenomenon of yielding occurs. Theoretically, this is the point at which the strain-stress curve begins to lose its linearity, as indicated by the point p in Figure 2.8. However, the transition from linearity to non-

linearity is gradua1 and it is difficult to determine the point precisely. As a consequence, a convention has been established to find the yield strength of a particular material: a straight line is to be constructed parallel to the elastic portion of the strain-stress curve at some specified strain offset, typically 0.002. The stress corresponding to the point at which this line intersect with the strain-stress curve is defined as the yield stress σ_y as indicated in Figure 2.8.

The yield strength of a material is a direct indication of its hardness. For crystalline materials, their hardness has been empirically established to be as about three times the yield strength [33]:

$$H = 3\sigma_y \tag{2.14}$$

Where this stress is termed the critical resolved shear stress σ_y, and it can be used to determine the yield stress σ_y, and subsequently the hardness of a material.

The hardness of the multilayer of very thin order can be calculated from the nanoindentation experiment. In nanoindentation small loads and tip sizes are used, so the indentation area may only be a few square micrometres or even nanometres. This presents problems in determining the hardness, as the contact area is not easily found. Atomic force microscopy or scanning electron microscopy techniques may be utilized to image the indentation, but can be quite cumbersome. Instead, an indenter with a geometry known to high precision (usually a Berkovich tip, which has three-sided pyramid geometry) is employed. During the course of the instrumented indentation process, a record of the depth of penetration is made, and then the area of the indent is determined using the known geometry of the indentation tip.

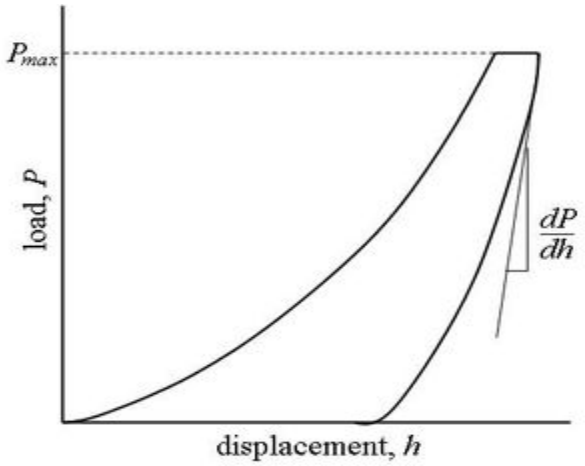

Figure-2.9: The load-displacement curve for the hardness measurement.

While indenting various parameters, such as load and depth of penetration, can be measured. A record of these values can be plotted on a graph to create a load-displacement curve (such as the one shown in Figure 2.9). These curves can be used to extract mechanical properties of the material. Modulus of elasticity: The slope of the curve, dP / dh, upon unloading is indicative of the stiffness S of the contact. This value generally includes a contribution from both the material being tested and the response of the test device itself. The stiffness of the contact can be used to calculate the reduced modulus of elasticity E_r.

$$E_r = \frac{1}{\beta}\frac{\sqrt{\pi}}{2}\frac{S}{\sqrt{A(h_c)}} \tag{2.15}$$

where $A(h_c)$ is the area of the indentation at the contact depth h_c (the depth of the residual indentation), and β is a geometrical constant on the order of unity. The reduced modulus E_r is related to the modulus of elasticity Es of the test specimen through the following relationship from contact mechanics:

$$\frac{1}{E_r} = \frac{(1-\upsilon^2{}_i)}{E_i} + \frac{(1-\upsilon^2{}_s)}{E_s} \tag{2.16}$$

Here, the subscript i indicates a property of the indenter material and ν is Poisson's ratio.

The hardness of a multilayer is not only regulated by its periodicity, but is also modified by the elastic moduli difference between the two constituent materials. Materials with larger elastic moduli generally have stronger inter-atomic binding. It is more difficult for dislocations to form and move in these materials and therefore they exhibit greater hardness. The total hardness of a multilayer can be characterized by three parts:

$$H = H_m + H_G + H_\Lambda \tag{2.17}$$

Where H_G is the part from the moduli modification; H_Λ, is the part resulting from periodicity modification, H_m is the part from the rule of mixture. The rule of mixture value of the hardness of a multilayer is the weighted average (usually on the basis of volume) of the hardnesses of individual copper and nickel films. Suppose the thicknesses of layer A and B are l_A, and l_B, respectively, the rule of mixture value of the hardness of the A/B multilayer is given by: In the case of equal thicknesses of the two layers, i.e., l_A, $= l_B$, the rule of mixture value of the multilayer is simply the average of the hardnesses of the two materials:

$$H_m = \frac{1}{2}(H_A + H_B) \tag{2.18}$$

The above analysis wsa done with a microphotonics NANOVIA series attached with aN AFM probe. This table also contains the hardness values measured on copper and nickel bilayer thin films deposited on the graphite surface and the trilayer of Ni/Cu /Ni on graphite and copper substrate electro-deposited from the same bath used for the multilayer samples for comparison.

2.1.5. SEM Analysis

In a typical SEM, electrons are thermionically emitted from a tungsten filament cathode and are accelerated towards an anode. Tungsten is normally used in thermionic electron guns because it has the highest melting point and lowest vapour pressure of all metals, thereby allowing it to be heated for electron emission. The electron beam, which typically

has an energy ranging from a few hundred eV to 40 keV, is focused by one or two condenser lenses into a beam with a very fine focal spot sized 0.4 nm to 5 nm. The beam passes through pairs of scanning coils or pairs of deflector plates in the electron column, typically in the final lens, which deflect the beam horizontally and vertically so that it scans in a raster fashion over a rectangular area of the sample surface.

When the primary electron beam interacts with the sample, the electrons lose energy by repeated scattering and absorption within a teardrop-shaped volume of the specimen known as the interaction volume, which extends from less than 100 nm to around 5μm into the surface. The size of the interaction volume depends on the electron's landing energy, the atomic number of the specimen and the specimen's density. The energy exchange between the electron beam and the sample results in the reflection of high-energy electrons by elastic scattering, emission of secondary electrons by inelastic scattering and the emission of electromagnetic radiation which can be detected to produce an image, as described below. Electronic devices are used to detect and amplify the signals and display them as an image on a cathode ray tube in which the raster scanning is synchronized with that of the microscope. The image displayed is therefore a distribution map of the intensity of the signal being emitted form the scanned area of the specimen. The image may be captured by photography from a high resolution cathode ray tube, but in modern machines is digitally captured and displayed on a computer monitor. Magnification in an SEM can be controlled over a range of about 5 orders of magnitude from x25 or less to x 250,000 or more. Unlike optical and transmission electron microscopes, image magnification in the SEM is not a function of the power of the objective lens. SEMs may have condenser and objective lenses, but their function is to focus the beam to a spot, and not to image the specimen.

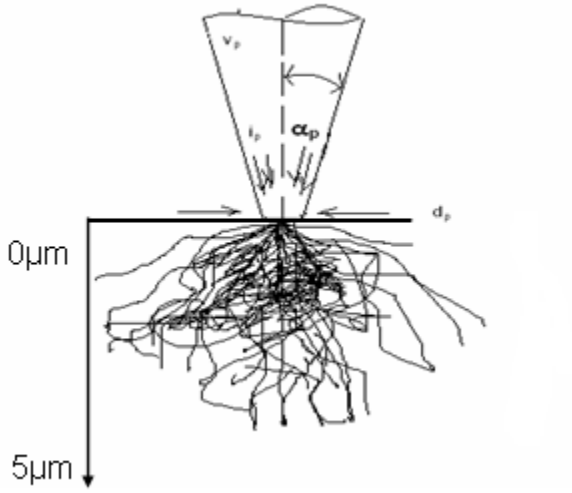

Fig-2.10: Interaction volume for a 20 Kev beam

.

Provided the electron gun can generate a beam with sufficiently small diameter, an SEM could in principle work entirely without condenser or objective lenses, although it might not be very versatile or achieve very high resolution. In an SEM, as in scanning probe microscopy, magnification results from the ratio of the dimensions of the raster on the specimen and the raster on the display device. Assuming that the display screen has a fixed size, higher magnification results from reducing the size of the raster on the specimen, and vice versa. Magnification is therefore controlled by the current supplied to the x, y scanning coils, and not by objective lens power.

Microscopic studies to examine the morphology, particle size and microstructure were done by a JEOL 6480 LV scanning electron microscope (SEM) equipped with an energy dispersive X-ray (EDX) detector of Oxford data reference system. Micrographs are taken at suitable accelerating voltages for the best possible resolution using the secondary electron imaging.

2.1.6. AFM analysis

The AFM consists of a microscale cantilever with a sharp tip (probe) at its end that is used to scan the specimen surface. The cantilever is typically silicon or silicon nitride with a tip radius of curvature on the order of nanometers. When the tip is brought into proximity of a sample surface, forces between the tip and the sample lead to a deflection

of the cantilever according to Hooke's law. Depending on the situation, forces that are measured in AFM include mechanical contact force, Van der Waals forces, capillary forces, chemical bonding, electrostatic forces, magnetic forces (see Magnetic force microscope (MFM)), Casimir forces, solvation forces etc. As well as force, additional quantities may simultaneously be measured through the use of specialised types of probe (see Scanning thermal microscopy, photothermal microspectroscopy, etc.). Typically, the deflection is measured using a laser spot reflected from the top of the cantilever into an array of photodiodes. Other methods that are used include optical interferometry, capacitive sensing or piezoresistive AFM cantilevers. These cantilevers are fabricated with piezoresistive elements that act as a strain gauge. Using a Wheatstone bridge, strain in the AFM cantilever due to deflection can be measured, but this method is not as sensitive as laser deflection or interferometry. Depending on the position of the tip and sample analysis requirement, their can be either contact or non-contact mode of operation. Traditionally, the sample is mounted on a piezoelectric tube that can move the sample in the *z* direction for maintaining a constant force, and the *x* and *y* directions for scanning the sample. Alternatively a tripod configuration of three pizo crystals may be employed, with each responsible for scanning in the x, y and z directions this eliminates some of the distortion effects seen with a tube scanner. The resulting map of the area s=f(x ,y) represents the topography of the sample.

SIEKO SPA 400 atomic force microscope (AFM) with a silicon probe is used to take the AFM figures. The micrographs presented here are in non-contact imaging mode.

2.1.7. Resistivity and GMR Analysis

The purpose of the 4-point probe is to measure the resistivity of any semiconductor material. It can measure either bulk or thin film specimen, each of which consists of a different expression. The derivation will be shown in this tutorial. The 4-point probe setup used in the EECS 143 instructional lab consists of four equally spaced tungsten metal tips with finite radius. Each tip is supported by springs on the other end to minimize sample damage during probing. The four metal tips are part of an auto-mechanical stage which travels up and down during measurements. A high impedance

current source is used to supply current through the outer two probes; a voltmeter measures the voltage across the inner two probes (Figure 2.11) to determine the sample resistivity. Typical probe spacing s ~ 1 mm.

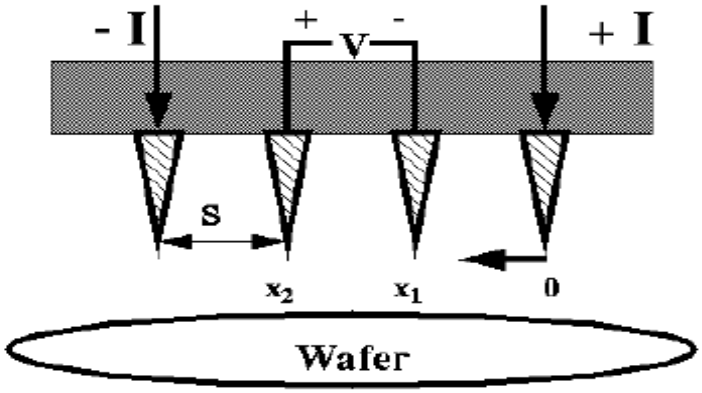

Figure-2.11. Schematic of 4-point probe configuration

The same instrument was used in the presence of magnetic field and the resistance variation was studied in the presence of magnetic field in transverse and longitudinal direction of the multilayer deposition .The average value of magnetic field was find out for the sake of convenience ,giving rise the value of the magnetoresistance of the sample.

2.2. Equipment-Process and Mechanism

In this work we have tried different baths like sulphate bath chloride bath, Watts bath and sulfamate bath. The bath composition of the electrolyte metal salts for all the baths are given in Table-2. The chemicals supplied (LOBA Chemie) were all of analytical grade. Doubly distilled was used for the preparartion of solution.

Table 2.1

Bath Type	Chemical	Concentration (g l^{-1})
Sulphate Bath	Nickelsulphate	280
	Copper sulphate	2
	Boricacid	8
	Sodiumchoride	10
Chloride bath	Nickel chloride	200
	Sodium chloride	36.88
	Boric acid	8
	Copper sulphate	8
Watts bath	Nickel sulphate	200
	Nickel chloride	36
	Boric acid	24
Sulfamate Bath	Nickelsulfamate	1.4lt
	Copper sulphate	3.12
	Boric Acid	31.2

The laboratory setup for electrodeposition has an electrolytic bath maintained at a particular composition with cathode and anode immersed in the bath. The anode is made out of copper and graphite, the cathode is a well polished material of Cu or graphite where the deposition will be done. The saturated calomel electrode (SCE) is used as the reference electrode. The key variables of the electrodeposition include temperature of the bath and the current density. These can be manipulated in achieving the required grain size in nanocrystalline range. The instrument used for the deposition is, Autolab PGSTAT 12 supplied by Echochemie, Netherland. The control over the grain size morphology and crystal structure mainly done by the control over the current density and temperature, those parameters are taken as the variables for our proposed nano multilayer deposition of the present work. Application of ultrasound increases the mass transport, nucleation and hinders the growth, giving the way towards the so wanted crystallinity of

nanostructure. The sonicator for the application of ultrasound used was EI2LH of 30 KHz and 60 watts power supply.

Cyclic voltametry tests were conducted from the solution to set the final operating parameters for the deposition. Multilayer deposition was done by the two pulse chrono amperometric technique. The current set for nickel and copper were 225 mA and 8 mA respectively. The time for the deposition was set according to the desired thickness range. Deposition were washed properly with distilled water and then dried by a drier for avoiding surface contamination. The experimental arrangement is shown in fig. 2.12.

Fig- 2.12.Photograph of the experimental setup instrument

CHAPTER – 3

Results & Discussion

Results and discussion

3.1. Selection of electrolyte

A critical topographical surface analysis has been done for choosing the most appropriate electrolyte for the multilayer deposition. The topographical images are shown in figure 3.1 all the surface images are in presence of ultrasound.

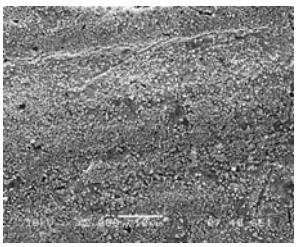

Fig-3.1(a)

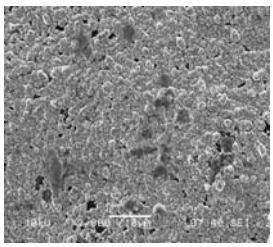

Fig-3.1(b)

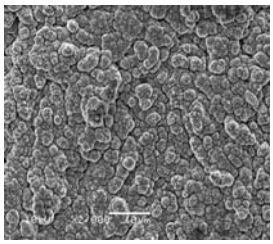

Fig-3.1(c)

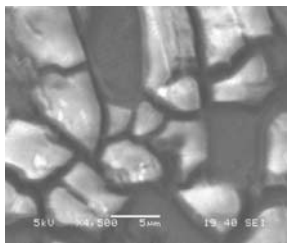

Fig-3.1(d)

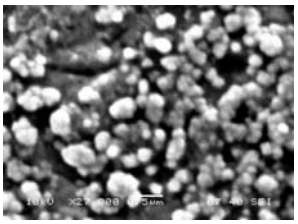

Fig-3.1(e)

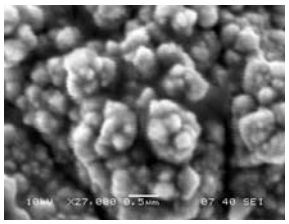

Fig-3.1(f)

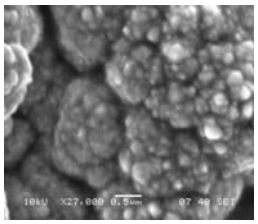

Fig-3.1(g)

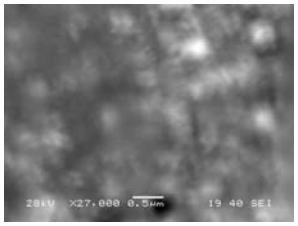

Fig-3.1(h)

It can be observed from the figure that the surface finish from chloride bath appears to be smooth at macroscopic level. But the magnified images indicate that the deposit from watts solution is more compact and seems to be free from any residual stress, the typical nickel electrodeposit which is seen from the sulfamate bath. So for further experimentation watts bath is chosen.

3.2. Electrochemical analysis

Figures 3.2 represent the cyclic voltammetry (CV) analysis of individual metals as well as for both the metals from the single bath. Figure 3.2 represents the CV analysis of copper and nickel. CV of copper was taken alone from a bath of 10 g l^{-1} Cu and 40 g l^{-1} (rest water) without the presence of Ni ions. Measurement has been taken at an OCP of 0.201 V. Sufficient time has been given to stabilize the OCP. The cycle has swiped in between the redox potential of copper i.e. −0.3 V to +0.5 V. It can be seen that deposition starts at around +0.025 V and has been extended to the final vertex potential of the negative sweep, but there is no sharp minima for the deposition as there is a continuous

ion supply to the electrode. In the positive potential run, the oxidation peak comes around +0.296 V with a zero current at a potential of +0.35 V, indicating complete dissolution

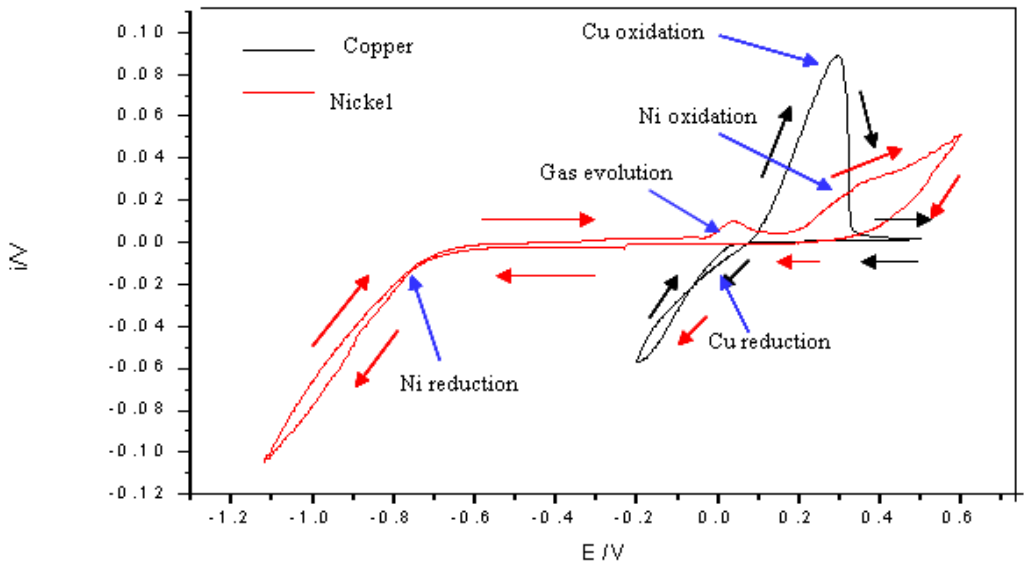

Figure-3.2: Cyclic voltammetry showing the Cu and Ni voltagram

of the deposited copper. The CV also shows no gas evolution. Comparing the CV for Nickel redox reaction from watts bath in absence of copper ions, it can be observed that like copper reduction there is no sharp reduction peak. And the deposition starts at a overpotential of − 0.7 V and has been extended to the complete negative vertex potential. In the upper potential, there is a small peak at around + 0.036 V and again there is an increase of current form the potential of + 0.226 V indicating the start of nickel dissolution. Figure 3.3 shows the CV for both the metals at a temperature of 55˚C in silent as well as sonication conditions. The sweep was done for the redox potential range of − 1.5 V to + 2 V for complete analysis of both the metals. For deposition of nickel it can be seen that the current flown at the final negative vertex potential is 350 mA in US field as compared to 200 mA of silent deposit. The cycle in US condition appears to be charge transfer controlled [34]. The gas evolution peak appears in both the cases. In sonication condition the peak has shifted to high overpotential region as observed by.

Sharp nickel dissolution peak can be observed in the CV plot. There is no sharp appearance of copper deposition or dissolution peak in the test because of the low concentration of the ions. However a CV has been conducted to confirm the copper redox reaction as shown in figure 3.2.

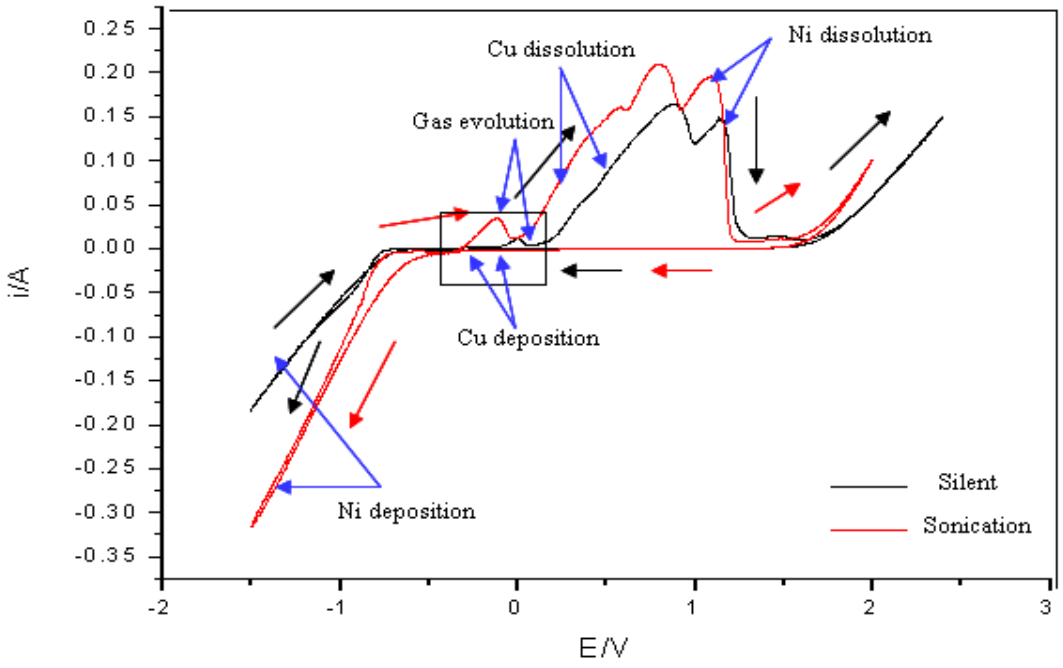

Figure-3.3:Showing cyclic voltammogram at 55ºC

The potential is varied in between − 0.7 V to 1.5 V. The voltammogram confirms copper reduction from − 0.17 V to − 0.6 V and showing a maximum at around − 0.35 V. the current observed form the peak potential is around 4 mA. And the reduction peak along with the gas evolution peak is clearly observed. Gas evolution peak is absent in the CV of copper from pure copper solution confirming the fact that the primary peak in figure 3.3 is from gas evolution only. Here the copper oxidation peaks are prominent. Hence as the dissolution peaks of both the metals are nearly same, the peaks have overlapped showing a single peak for both the metals.

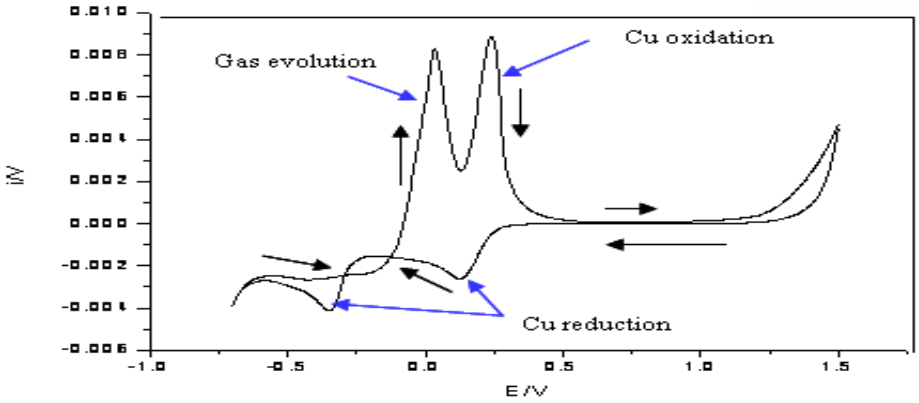

Figure-3.4: Showing the CV for single bath deposition at 30ºC

Figure 3.4.shows CV for the single bath deposition at 30˚C. Current flown at the final potential is nearly same for silent as well as sonication conditions. But the fact that

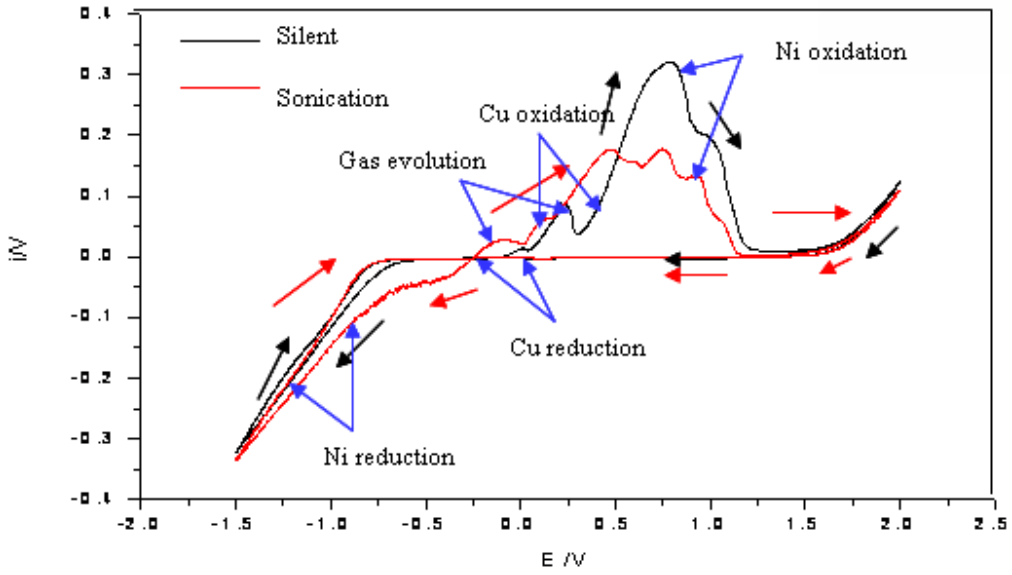

Figure-3.5: CV of Cu and Ni in silent and sonication condition.

low temperature nickel deposition from watts solution leads to black nickel deposition has been solved by application of ultrasound, as explained in the next section. Like the voltammogram form the high temperature region, it also contains the same valleys and peaks but the position has been shifted towards negative directions.

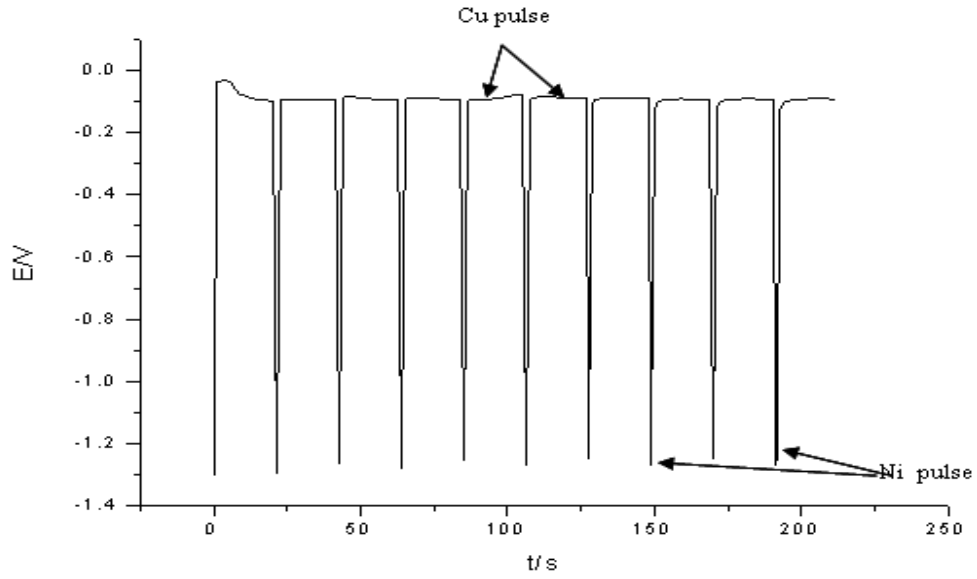

Figure-3.6:Chronopotentiometry for Cu and Ni.

Based upon the above observations we have chosen chrono potentiometry methods to control the thickness of each of the layers. As explained earlier 1:100 of metal ratio is maintained to obtain pure layers rather alloy layers. Figure 3.6 shows plot of the deposition.Current pulses and time duration chosen are 225 mA and 4 mA & 0.2 s and 20 s for Ni and Cu respectively.

3.3. Phase and surface analysis

Figure 3.7. shows the XRD phase analysis of the deposit at room temperature in both conditions. The diffraction peaks corresponding to 2θ = 43.298, 50.434, 74.132 are copper peaks having the JCPDS card no. 04-0836. Similarly for nickel the peaks are of 2θ = 44.497, 51.850, 76.383 having the JCPDS card no. 87-0712. from the plot it can be observed that the peaks are sharp for both the metals indicating the high crystallinity of the metallic phases. However the intensity of nickel phase in silent conditions are not prominent. The fact behind the observation may be that the deposition is not appropriate in silent condition at room temperature. Figure 4.7(c) and (d) showing the deposition of watt's bath in the presence of ultrasound i.e. in the sonication condition at low temperature and low temperature respectively.

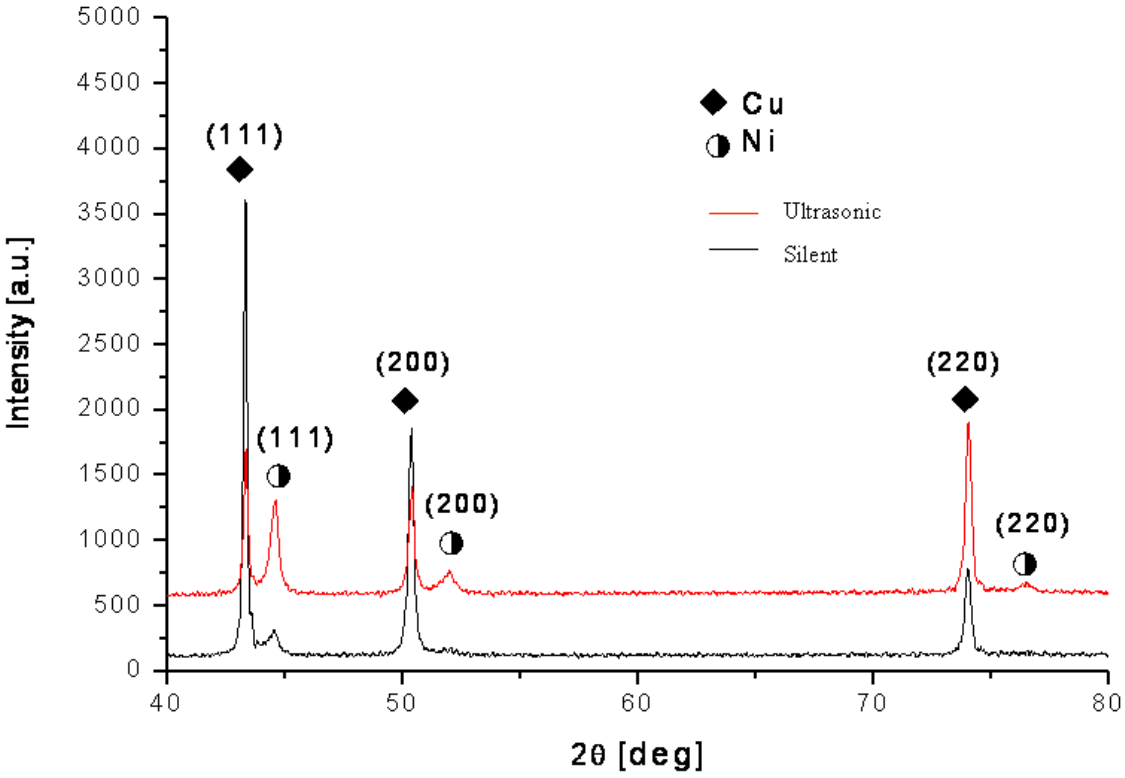

Figure 3.7(a) and (b) showing the deposition from the watt's bath in silent condition at high temperature and low temperature respectively .In the high temperature the deposition for watt's bath showing almost spherical grains with greater surface finish, comparison to the low temperature deposition. The deposition at low temperature showing dendritic structure, unusual growth of the grains with less surface finishing comparison to the high temperature deposition .But at high temperature deposition showing the grains fine order as compare to the low temperature deposition. High temperature deposition showing powdery deposition and low temperature deposition showing the irregular crystallinity. Presence of void space in both the silent deposition but the value showing higher order at high temperature deposition. At high temperature deposition (fig-3.2(b)) the grains are showing the cumulative growth with the deposition condition. The grains are showing almost coarser in size.

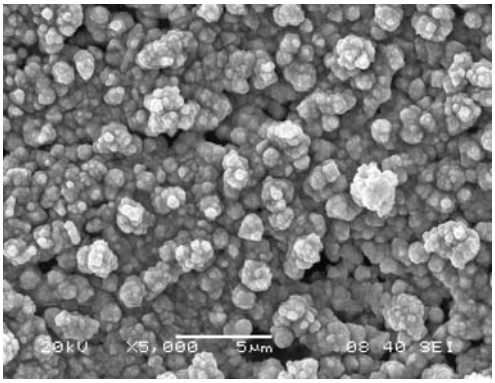

Figure-3.7(a)

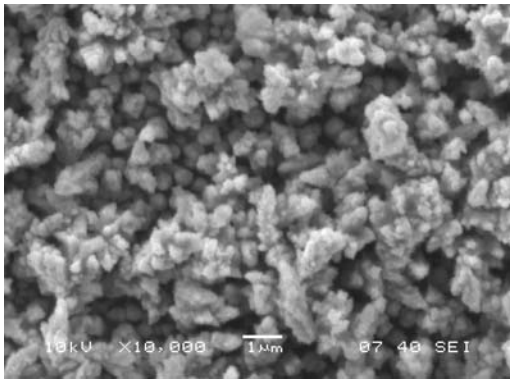

Figure-3.7(b)

Figure 3.7(c) and (d) showing the deposition of watt's bath in the presence of ultrasound i.e. in the sonication condition at low temperature and low temperature respectively. Figure 3.7(c) for high temperature watt's bath in sonication condition showing higher surface finish, smooth surface, crystalline form with the requirement of finer grains with compact structure comparison to the figure 3.7(a) at silent condition.

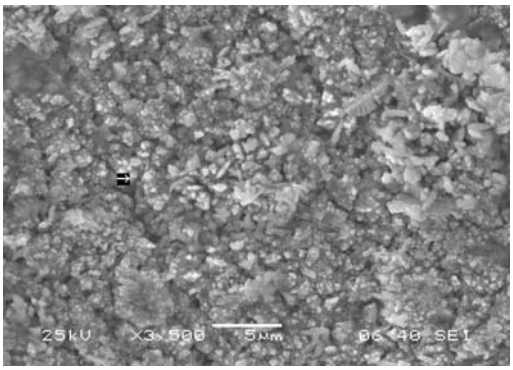

Figure-3.7(c)

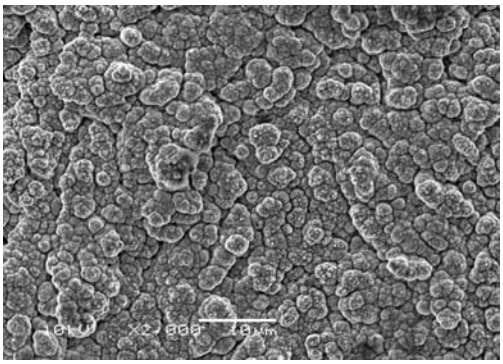

Figure-3.7(d)

Figure 3.7(d) i.e the low temperature deposition in presence of ultrasound in comparison to the figure 3.7(b) (silent) showing the grains almost spherical, finer, high surface smooth, minimized void space with the consecutive grains sintered to give the compact crystalline surface. Comparison to the low temperature silent and ultrasonic conditions the, sonication condition showing higher compact and uniform structure. Comparison to figure 3.7(c) the structure showed in figure 3.7(d) gives the less compact but the higher uniform ,cauliflower structure of different sizes are observed. The formation of cauliflower structure due to the increase in uniform deposition rate in presence of ultrasound at low temperature. The structure showed in Figure3.7(d) showing the grain boundaries are almost coalescence with each other.

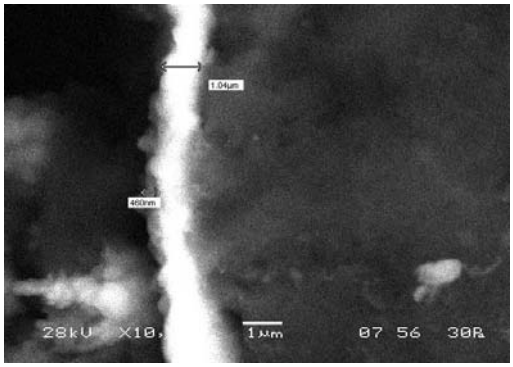

Figure-3.7(e)

Figure 3.7(e) showing the multilayered structure is observed as a periodical structure. The multilayer showing the positive curvature in the growth direction with an abrupt change at grain boundaries The typical waviness resulting from the growth related curvature of the sublayer within the grains .The sublayer are not curved due to the fact that the dimension of each layer sublayer is of the same order as the grain size. Thus the grain boundary does not distort the growth front of the deposit.

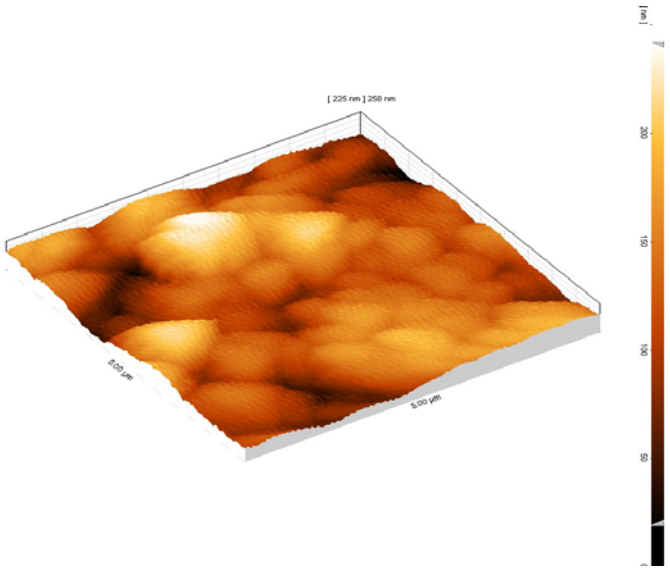

Figure-3.8: AFM 3-D dynamic mode image of the top surface of the multilayer.

The comprehensive analysis of AFM topographic images has been performed with emphasis on important parameters for such mirrors, the surface roughness, for nanometric and micrometric areas, involving AFM tips with different radius of curvature. The analyses revealed a high quality of the deposited mirrors. These graphs (Figure 3.8)

mean that the surface of our reflectors can be considered as a smooth surface with a roughness having the same average spectrum over the surface. This result gives more strength to our overall conclusions regarding the real quality of the deposited mirrors. Although the roughness decreases after deposition, the distribution of the substrate roughness has an important influence over the distribution of the multilayer surface roughness, the disposing of the roughness being similar for both.

3.4. Texture analysis

Figure 3.9. represents the texture analysis of the deposits with their respective ODF data with nickel top and copper top surfaces deposit to correlate the hardness data with the preferred oriented planes. The pole figures with their corresponding scattered orientation levels are represented clearly in figure.

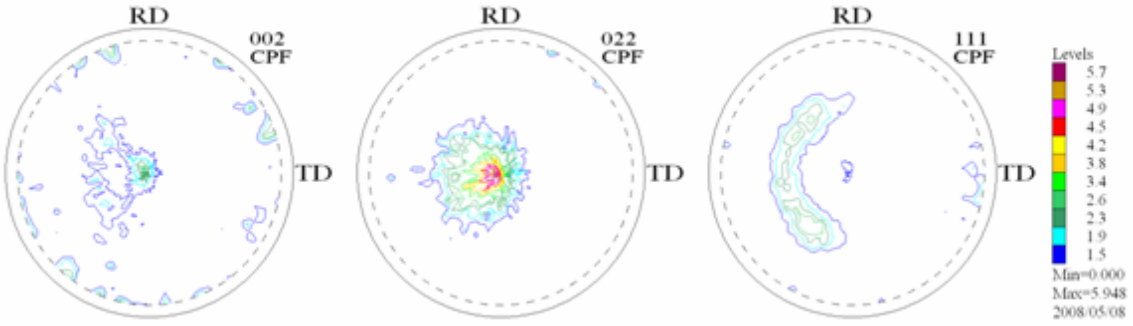

Fig. 3.9.(a) Pole figure of nickel deposit

(022) plane is having the highest scattered orientation where as (111) plane is having the least one. So we conclude that the nickel ions have arranged themselves to grow in the most favorable plane, the highest packing plane i.e. (111). Fig. 3.9.(b) represents the ODF to the above analyzed data.

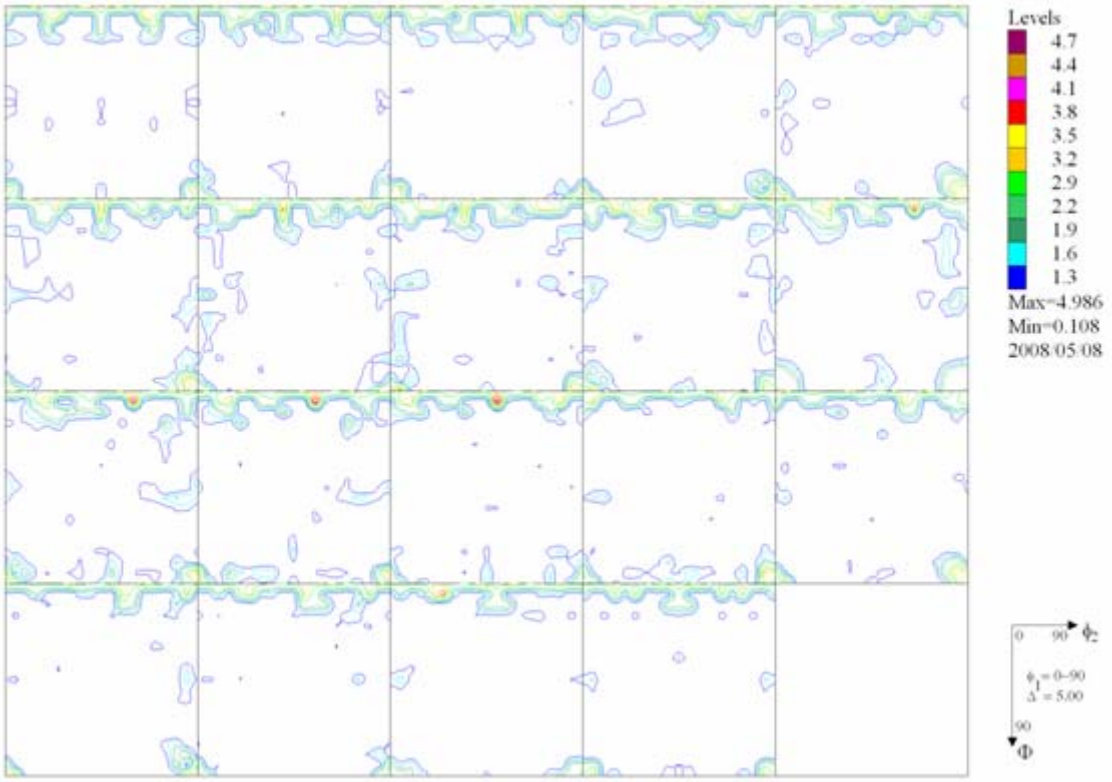

Fig. 3.9.(b) ODF of Nickel deposit

In same fashion if the pole figure for copper deposit is analyzed it can be observed that like nickel (111) plane has the least scattered orientation leading to a compact and dense mass in the same plane.

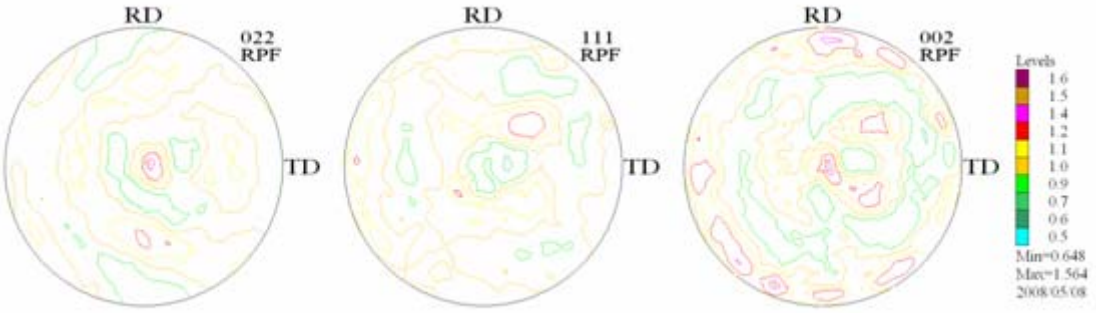

Fig. 3.9.(c) Pole figure for copper deposit

And figure 3.9.(c) represents the ODF of above calculated values.

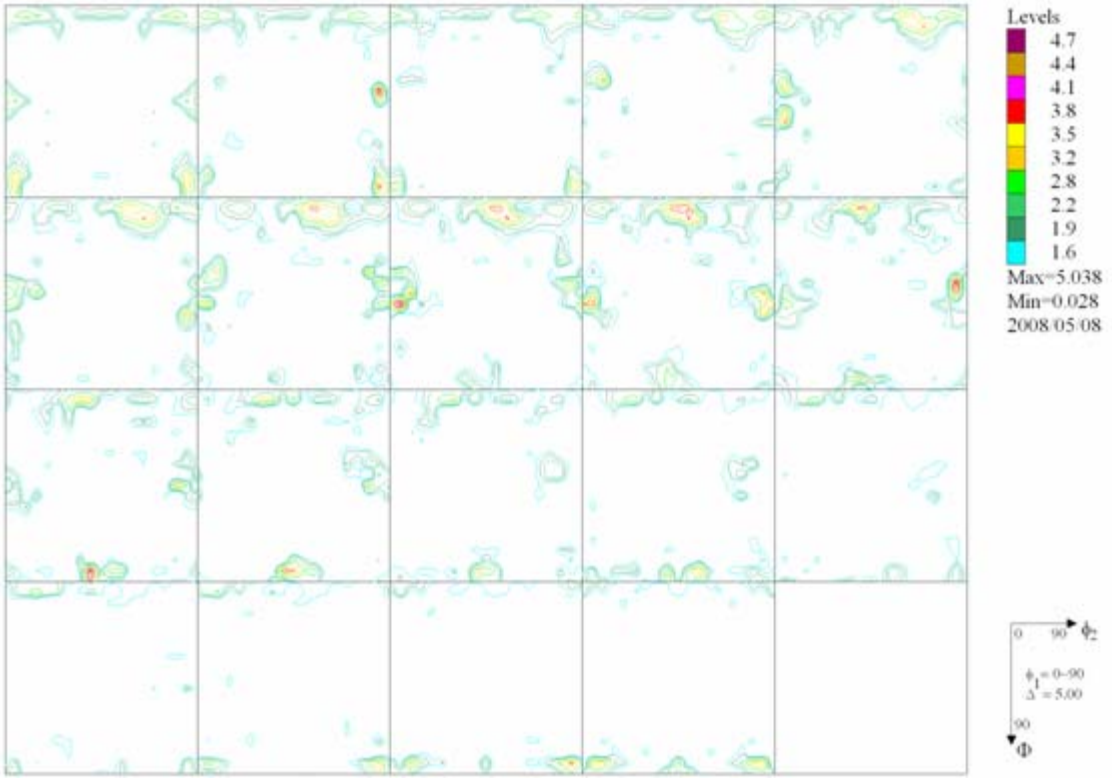

Fig. 3.9.(d) ODF of Copper deposit.

3.5. Hardness results

Hardness values are outputted directly by the software. The software also produces loading and unloading curves, and the hardness depth curves as presented in figure 3.11 and 3.12 for several samples.

The average hardness values of the samples are presented in Table -3. it can be observed that the bilayer has a hardness value higher than the individual values of the metallic deposits. And the trilayer has even higher value than the bilayers. To study the substrate effects we have compared the hardness values onto a copper susbstrate. It shows the prominent substrate effect on the strength of the multilayers deposited. Figure 3.10 showing the hardness value of the bilayer showing the higher order almost average of the hardness of the single layers of copper and nickel.

Table-3.1 Measured hardness values of Cu/Ni multilayer systems

Item	Copper	Nickel	Cu/Ni bilayer	Ni/Cu/Ni layer	Ni/Cu/Ni (on copper)
H in GPa	0.205	0.513	1.884	2.8204	3.5585
E in GPa	9.913	15.864	48.162	67.1657	186.8215

The slope of the uploading graphs giving the value of the elastic modulus value of the bilayer is the average of the elastic modulus of the single layers.

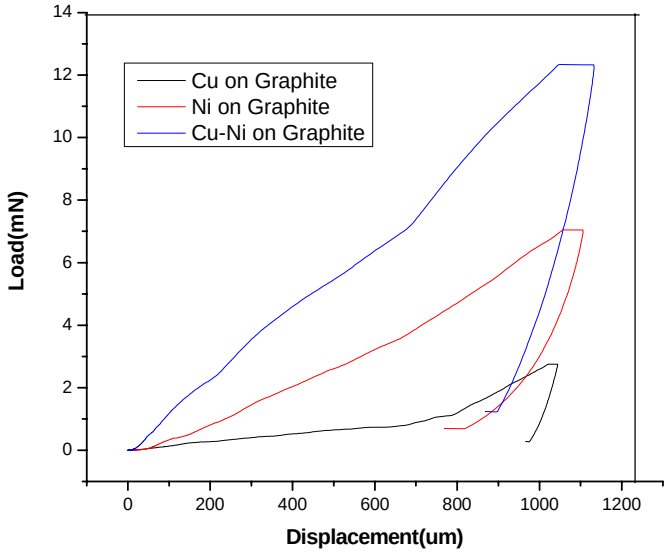

Figure 3.10: Load-Unloading curve for copper, nickel and copper-nickel bilayer.

The load–unloading graph for Ni-Cu-Ni trilayer on graphite substrate and copper substrate are shownin the figure 3.11.The graphs showing the same result as predicted from the theoretical prediction.The trilayer formation on copper substrate giving higher order hardness compairision to the trilayer deposition on graphite substrate.The results mathches with the results of the XRD result of the superlattice formation on the copper substrate.

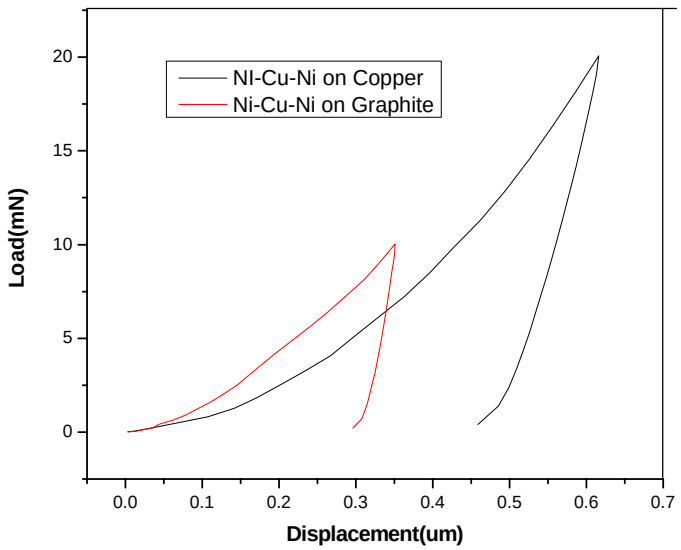

Figure 3.11: Load-Unloading graph for trilayer of Ni-Cu-Ni on copper and graphite substrate.

3.6 Resistivity and GMR Analysis

The GMR measurement was done using the four point contact method by using the instrument EECS 143 model. The external magnetic field application arrangement was done with it. The multilayer sample prepared in presence of ultrasound was investigated for the GMR measurement. In absence of magnetic field the variation of the current with potential is ohmic as shown in the graph of figure 3.12.

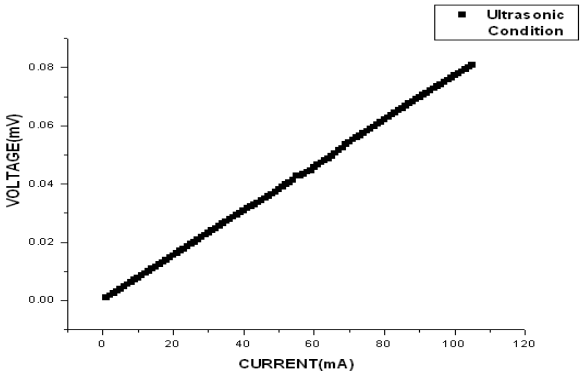

Figure 3.12: Linear ohmic variation in absence of magnetic field.

As the magnetic field is applied in the direction in the longitudinal direction of the multilayer sample the variation of the resistance with the presence of magnetic field as

shown in figure 3.13(a).The magnetic resistance value of the multilayer sample deposited at silent condition and low magnetic field showing magneto resistance variation, but not giving the giant value. This results matches with the previous result of the interfacial irregularities at silent condition of the deposit giving rise to the low variation of the magnetoresitance. Since the interface plays an important role in the variation of the magnetoresitance during the spin pinning state from one layer to the other the interfacial irregularity hamper the pinning percentage so as to the magnetoresistance. Figure 3.13(b) gives the variation of the magnetoresitance variation of giant value at the ultrasonic condition. As established from the previous data the presence of ultrasound gives the cleaner and coherent interface .So due to the presence of cleaner and coherent interface the spin pinning from one layer to the other will be easier depending on the spin orientation of the consecutive nickel layers. Comparing the graphs of figure3.13 (a) and (b),it can be investigated that in ultrasonic condition with higher magnetic field the magentoresistance variation showing 10 fold increase in the magneto resistance.

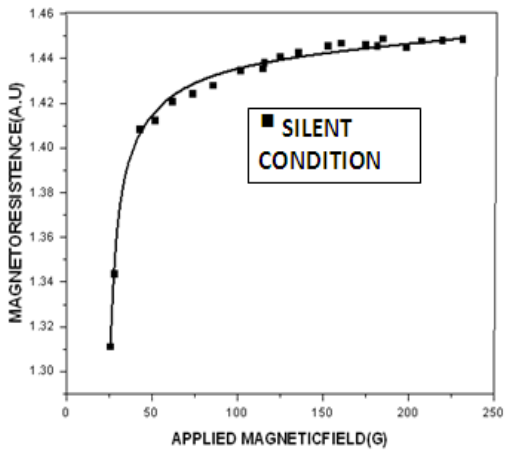

Figure 3.13(a)

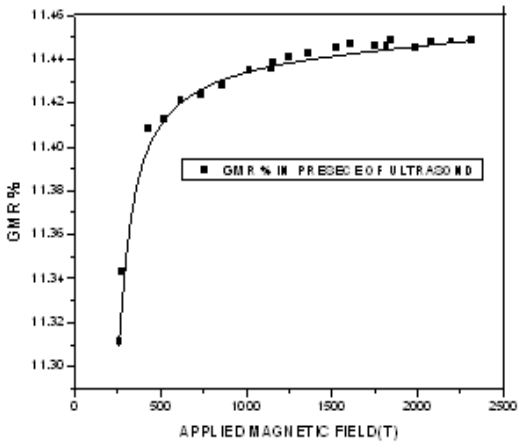

Figure 3.13(b)

Figure 3.13 GMR value versus longitudinal magnetic field in electrochemically grown Cu/Ni multilayer using direct current. (a)Magenotoresistace variation, (b)GMR variation.

CHAPTER – 4

Conclusions

4. Conclusions

Multilayered of Cu/Ni with a sublayer thickness in the nano order have been successfully sonoelectrochemically deposited from various baths like sulphate, chloride, suffamate and watt's bath. Because of the better surface finish watts bath has been chosen for experimentation. The multilayer thicknesses were crucially controlled by a well formulated mechanism by the potentiostatic and galvanostatic application. The phase analysis was done exclusively by XRD. Microstructure is characterized by SEM and AFM. Texture study was done by small angle X ray study. Hardness was done by a nanoindentor. And the magnetic properties were studied by the conventional four probe analysis method.

With a careful CV study the deposition current was chosen. The study showed that the appropriate current for nickel was 225 mA and for copper it was 4 mA.

The watts bath at different temperature showed difference in microstructure in sonicated and silent condition. As explained by various authors the deposit obtained at low temperature was black and appears to be powdery as compared to sonicated low temperature, giving better microstructure. The morphology is in micron and nanorange is confirmed by the microscopic analysis.

Hardness values are found to be enhanced with increased number of layers i.e. from a value of 0.205 GPa to 3.558 Gpa. The effect of different substrate like copper and graphite are investigated. The formation of multilayer over the copper substrate gives superlattice structure with enhanced hardness.

The GMR measurement at silent and ultrasonic condition gives several fold (10) increase in GMR value in sonicated condition.

References

1. Ludimila Eckertova, Physics of Thin Films, Plenum Press, 96 (1986)
2. Scott A. Barnett, Physics of Thin Films, 17, 2, (1993)
3. Blum W. Tram. Am. Electrochem. Soc. 40: (1921) 307-20
4. Tench DM, White JT., Metal Tram -4 15A: (1984)2039-40
5. Yahdom J, Zadak , J. Mater. Sci. 22: (1987)499-503
6. Robert A. Alberty, Robert J. Silbey, Physical Chemistry, John Wiley & Sons, inc.,243, (1992).
7. D Polk, R Siegel and B Kear (eds), M*ulticomponent Ultrafine Microstructures, Mater Res Soc symp.procmp Proc,132(1989)* Materials Research Society Pittsburg PA
8. Wolf, S. A., Awschalom, D. D., Buhrman, R. A., Daughton, J. M., von Molnár, S., Roukes, A. Y., Chchelkanova, A. Y. & Freger, D. M. Science 294, (2001) , 1488–1495.
9. Barthélémy, A., Fert, A., Contour, J.-P., Bowen, M., Cros, V., Teresa, J. M. D., Hamzic, A., Faini, J., George, J. M., Grollier, J., *et al.* (2002) J. Magn. Magn. Mater. 68**,** 242–245.
10. Prinz, G. A. (1998) Science 282**,** 1660–1663.
11. Grünberg, P., Schreiber, R., Pang, Y., Brodsky, M. & Sowers, H. (1986) Phys. Rev. Lett. 57**,** 2442–2445.
12. Baibich, M., Broto, J., Fert, A., Dau, F. N. V., Petroff, F., Eitenne, P., Creuzet, G., Friedrichi, A. & Chazelas, J. (1998) Phys. Rev. Lett. 61**,** 2472–2475.
13. Zangwill, A. Physics at Surfaces (Cambridge Univ. Press, Cambridge, U.K.), p. (1988) 428.
14. G.L.Katona,Z.Berenyi,L.Peter,K.Vad, Vacume (online)
15. U.S.Mohanty,B.C.Tripathy,P.Singh,S.C.Das,Minerals Engineering 15(2002)531-537.
16. Wie Zhang,Qunji Xue,Xushou Zhang,Wera 214(1998)74-78.

17. Laszlo Peter,Gabor L.Katona,Zoltan Berenyi,Kalaman Vad,Gabor A.Langer,Eniko Toth-Kadar,Jozer Pader,lajos Pogany,Imre Bakobyi,Electrochemical Acta(2007),
18. S.K.Ghose,P.K.Limaye,S.Bhattacharya,N.L.Soni,A.K.Grover,Surface and coating Technology 201(2007)7441-7448
19. D.k.Park,N.V.Myung,M.Schwartz,K.Nobe,Electrochemical acta,47(2002)2893-2900
20. Ch.bonhote and D.Landolt,Electrochemical Acta,Vol.42,No.15.pp.2407-2417,1997
21. Takeshi Miyake,Michiyuki Kume,Koichi Yamaguchi,Dinesh P.Amalnerkar,Thin Solid Films 397(2001) 83-89
22. E.Gomez,A.Labarta,A.Liorente,E.Valles,Electrochemical Acta 48(2003)1005-1013.
23. N.D.Telling,M.D.Crapper,D.R.Lovett,S.J Guifoyle,C.C.Tang,M.Petty,Thin solidfilm317(1998)278-281.
24. C.C.Tang,N.D.Telling,S.Langridge,Physics b248(1998)395-398
25. E.Gomez, A.Labarta, A.Llorente, E.Valles Surface and coating technology 153 (2002) 261-266.
26. M.Shima, L.Slamanca-Riba, R.D.McMichal and T.P.Moffat, J.Elect.Sco.149 (9) (2002)c439-c444.
27. A.Wawro, L.T.Baczewski, R.kalinowski, M.Aleszkiewicz, J.Rauluszkiewicz, Thin Solid Films 306(1997)326-330.
28. .M.Uhlemann,A.Gebert,M.Herrich,A.Krause,A.Cziraki,L.Schultz,Electrochemical.Acta 48(2003)3005-3011
29. Wei Zhang, Qunji Xue, Thin Solid Films 305 (1997) 292-296.
30. Peter Luger, Modem X-Ray Analysis on Single Crystals, W de G, 80, 1980
31. L.Gerward, S.Lehn, and G.Christiansen, Texture, Vol 2,(1976),95.
32. Watanabe T.,Nano Plating:Microstructure formation Theory of Plated films and a Data base of Plated films,Lavoisier,03-2004
33. D. Tabor, J. Inst. Met. 79, l(1951)

Michael E. Hyde, Richard G. Compton, J. Electroanal. Chem, 531